# A cytoskeletal clutch mediates cellular force transmission in a soft, three-dimensional extracellular matrix

Leanna M. Owen[a,b], Arjun S. Adhikari[b], Mohak Patel[c], Peter Grimmer[d], Natascha Leijnse[b], Min Cheol Kim[b], Jacob Notbohm[d], Christian Franck[c], and Alexander R. Dunn[b,*]

[a]Biophysics and [b]Chemical Engineering, Stanford University, Stanford, CA 94305; [c]School of Engineering, Brown University, Providence, RI 02912; [d]Department of Engineering Physics, University of Wisconsin–Madison, Madison, WI 53711

**ABSTRACT** **The ability of cells to impart forces and deformations on their surroundings underlies cell migration and extracellular matrix (ECM) remodeling and is thus an essential aspect of complex, metazoan life. Previous work has resulted in a refined understanding, commonly termed the molecular clutch model, of how cells adhering to flat surfaces such as a microscope coverslip transmit cytoskeletally generated forces to their surroundings. Comparatively less is known about how cells adhere to and exert forces in soft, three-dimensional (3D), and structurally heterogeneous ECM environments such as occur in vivo. We used time-lapse 3D imaging and quantitative image analysis to determine how the actin cytoskeleton is mechanically coupled to the surrounding matrix for primary dermal fibroblasts embedded in a 3D fibrin matrix. Under these circumstances, the cytoskeletal architecture is dominated by contractile actin bundles attached at their ends to large, stable, integrin-based adhesions. Time-lapse imaging reveals that α-actinin-1 puncta within actomyosin bundles move more quickly than the paxillin-rich adhesion plaques, which in turn move more quickly than the local matrix, an observation reminiscent of the molecular clutch model. However, closer examination did not reveal a continuous rearward flow of the actin cytoskeleton over slower moving adhesions. Instead, we found that a subset of stress fibers continuously elongated at their attachment points to integrin adhesions, providing stable, yet structurally dynamic coupling to the ECM. Analytical modeling and numerical simulation provide a plausible physical explanation for this result and support a picture in which cells respond to the effective stiffness of local matrix attachment points. The resulting dynamic equilibrium can explain how cells maintain stable, contractile connections to discrete points within ECM during cell migration, and provides a plausible means by which fibroblasts contract provisional matrices during wound healing.**

**Monitoring Editor**
Manuel Théry
CEA, Hopital Saint Louis

Received: Feb 13, 2017
Revised: May 26, 2017
Accepted: May 31, 2017

## INTRODUCTION

Cell-generated mechanical forces and the resulting deformation of the surrounding extracellular matrix (ECM) are essential aspects of cell migration, differentiation, and proliferation and hence play a vital role in the development and repair of biological tissues (Krieg *et al.*, 2008; Wozniak and Chen, 2009; Mammoto *et al.*, 2013). Historically, models for how cells transmit cytoskeletal forces to their surroundings have been derived from observations of cells adhering to continuous, two-dimensional (2D) surfaces (Gardel *et al.*, 2010). However, the tissue microenvironment experienced by cells in vivo is three-dimensional (3D), fibrous, and confining (Schwartz and Chen, 2013). Whether the mechanisms of cytoskeletal force generation described for cells adhering to flat, hard surfaces are conserved in more biologically realistic 3D matrices is not firmly established due principally to the technical challenges inherent in quantifying

This article was published online ahead of print in MBoC in Press (http://www.molbiolcell.org/cgi/doi/10.1091/mbc.E17-02-0102) on June 7, 2017.

*Address correspondence to: Alexander R. Dunn (alex.dunn@stanford.edu).

Abbreviations used: ECM, extracellular matrix; FA, focal adhesion.

matrix and cytoskeletal dynamics for cells in fully 3D model systems.

Work over several decades has resulted in detailed models of how the actomyosin network transduces force to stiff, continuous, 2D surfaces (Harris *et al.*, 1980; Oliver *et al.*, 1995; Waterman-Storer *et al.*, 1998; Franck *et al.*, 2011). Under these circumstances, cells commonly generate a flat leading edge in which actin polymerization in the lamellipodium and myosin contractility combine to generate a continuous flow of the actomyosin cytoskeleton from the cell edge toward the cell body (Giannone *et al.*, 2004, 2007; Ponti *et al.*, 2004; Burnette *et al.*, 2011). The resulting retrograde actin flow is incompletely coupled to cellular adhesions, resulting in a velocity difference between actin, adhesion components, and the ECM, analogous to the differential motion within an automotive clutch (Lin and Forscher, 1995; Hu *et al.*, 2007; Alexandrova *et al.*, 2008; Gardel *et al.*, 2008; Aratyn-Schaus and Gardel, 2010). In this model, force transmission to the ECM results from a frictional drag between actin and the integrin-based adhesions and between integrins and the ECM. Although this overall mechanism of cellular force transduction is supported by many studies, variations exist (Salmon *et al.*, 2002). Of note, some cell types also exert tractions via contractile actomyosin bundles termed ventral stress fibers. In a third, indirect mode of force transduction, cytoskeletal contraction is generated in actomyosin bundles termed transverse arcs and transferred to adhesions via noncontractile actin bundles termed dorsal stress fibers (Livne and Geiger, 2016). Whether and, if so, how any of these mechanisms of force transduction function for cells in 3D matrices are, to our knowledge, not firmly established.

Previous studies support at least some underlying similarities for force transduction in 2D versus 3D environments. Fibroblasts, endothelial cells, and a variety of cancer cells cultured in 3D ECMs adopt a mesenchymal phenotype in which cells generate protrusions containing bundled actin and myosin and in some cases assemble adhesions containing paxillin, vinculin, and zyxin, canonical components of focal adhesions (Cukierman *et al.*, 2001; Tamariz and Grinnell, 2002; Kubow and Horwitz, 2011; Giri *et al.*, 2013; Thievessen *et al.*, 2015). In some studies, these adhesions, together with attached collagen fibrils, moved both toward and away from the tips of cellular protrusions, suggestive of a role in transducing force to the ECM (Petroll and Ma, 2003; Doyle *et al.*, 2015). Small-molecule inhibition experiments suggest that contractility generated by nonmuscle myosin II contributes to matrix deformation and contraction (Vishwanath *et al.*, 2003; Meshel *et al.*, 2005; Grinnell and Petroll, 2010; Kubow *et al.*, 2013). In sum, these studies indicate that key molecular components of the cell's force generation and transmission machinery are likely conserved across 2D and 3D environments.

Although the molecular components appear to be conserved, existing observations are equivocal as to whether current models of cytoskeletal force transduction can apply to cells in biologically realistic matrices. The observation that stress fibers commonly form in cells cultured on hard (e.g., glass) but not softer, ~1-kPa surfaces has led to debate on their physiological function (Burridge and Wittchen, 2013). However, bundled actin structures akin to stress fibers have been reported in fibroblastic cells during wound repair (Gabbiani *et al.*, 1972; Tomasek *et al.*, 2002) and are implicated in the progression of fibrotic disease (Hinz, 2012). More broadly, to our knowledge, the key element of molecular clutch model, namely a differential velocity between the actin cytoskeleton, adhesions, and the ECM, has not been reported for cells in a 3D environment. Whether retrograde flow can be established in cells embedded in fibrous matrices is also uncertain due to the discontinuous, porous nature of surrounding matrix.

In this study, we present a quantitative analysis of how cells in soft, 3D matrices transduce cytoskeletal force to the ECM. As a model system, we chose primary human foreskin fibroblasts (HFFs) embedded in a soft (~200 Pa) 3D fibrin network. Fibrin matrices are present in wounds and at the basal surface of tumors (Clark *et al.*, 1982; Schäfer and Werner, 2008). Fibroblast migration into and remodeling of these spaces leads to wound healing and remodeling of the cancer stem cell niche, respectively (Clark *et al.*, 1982; Schäfer and Werner, 2008). To understand how fibroblasts transduce cytoskeletal force in ECM, we tracked in three dimensions the deformation of a fluorescently labeled fibrin matrix. Characterization of the fibrin displacement around the cells and numerical simulations of the fibrin matrix revealed that HFFs generate substantial deformations corresponding to nanonewton forces along cellular protrusions.

To understand how these forces were generated, we used simultaneous 3D time-lapse imaging and quantitative tracking of the fibrin ECM, focal adhesions (FAs; labeled with paxillin or zyxin) and the underlying actin cytoskeleton (labeled with LifeAct or α-actinin-1). Enhanced green fluorescent protein (EGFP)–α-actinin-1 puncta on the actin cytoskeleton provided trackable, bright fiducials for long-term, high-resolution tracking of the actin cytoskeleton in three dimensions. These data revealed dynamic coordination between the motions of actin, focal adhesions, and the underlying substrate. We found that α-actinin-1 puncta within actomyosin stress fibers moved more quickly than the paxillin-rich adhesion plaques, which in turn moved more quickly than the local matrix, an observation reminiscent of the molecular clutch model. A subset of actin stress fibers continuously elongated at adhesion sites within protrusions, providing stable yet structurally dynamic coupling to the ECM.

These results provide a picture of a 3D clutch mechanism by which cells transmit force to their surroundings in a soft, 3D fibrin matrix. In the model system studied here, force transduction is mediated by stress fibers and FAs, structures not commonly associated with soft matrices but well studied in two dimensions. Analytical modeling and numerical simulation provide a plausible physical explanation for this result and support a picture in which cells respond not so much to the macroscale, bulk mechanical properties of the matrix as to the effective stiffness of the local matrix attachment points. We suggest that the stress fiber–based mechanism of force transduction observed here may allow fibroblasts to maintain persistent, contractile attachments to the matrix as they migrate through and remodel the ECM, a picture consistent with their physiological function.

## RESULTS

### HFFs generate retrograde and anterograde matrix displacements along protrusions

We embedded HFFs in a 2.25 mg/ml, ~200-Pa fibrin matrix. After allowing the cells to spread for 8–20 h, we simultaneously imaged the fibrin gel and fluorescent protein–tagged paxillin, α-actinin-1, F-actin, or myosin regulatory light chain (MRLC) with time-lapse confocal microscopy (Figure 1A). A number of strategies have been described to quantify matrix deformations and cell tractions (Bloom *et al.*, 2008; Legant *et al.*, 2010; Lesman *et al.*, 2014; Notbohm *et al.*, 2015b; Steinwachs *et al.*, 2016). Given the complex material architecture of fibrin gels and the lack of experimentally validated constitutive models for fibrous materials, we characterize cellular force generation through the associated ECM deformation fields. Of importance, kinematic descriptions of cellular force generation—that is, matrix displacements and strains—have similar biophysical

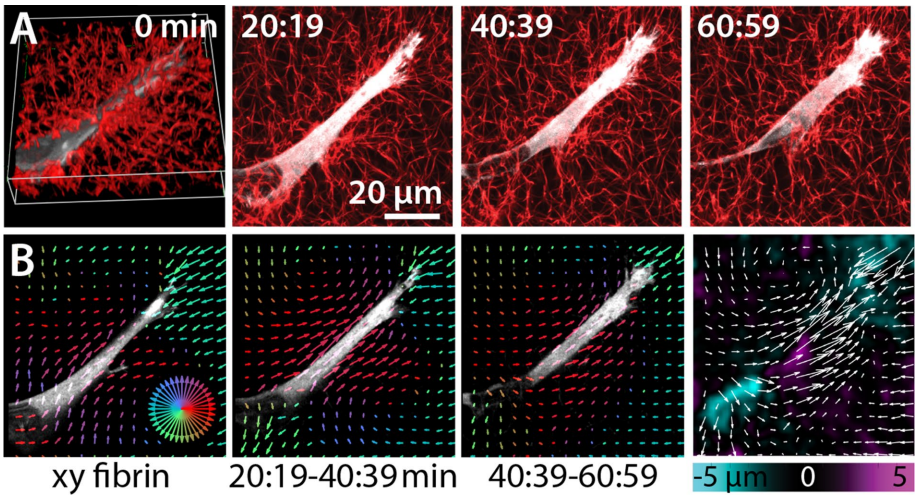


FIGURE 1: Fibroblast-generated displacements measured in a 3D fibrin matrix. (A) Confocal, time-lapse images of a dermal fibroblast migrating through a fibrin matrix. Left, 3D reconstruction of the cell and gel at time 0, followed by maximum intensity projections at later time points. (B) Matrix displacements as quantified using FIDVC. Left three panels, sample plots of the *x*- and *y*-components of fibrin displacement in one *z*-slice measured between sequential time points. The color of the arrow describes the angle of displacement, and the length is proportional to magnitude. Right, heat map depicting *z*-component of fibrin displacement at a sample *z*-slice at the last time point. Magenta is toward and cyan is away from the coverslip.

interpretations with regard to cell adhesion and migration compared with cell tractions, as we recently demonstrated (Stout *et al.*, 2016). We quantified and mapped matrix deformations in three dimensions using fast iterative digital volume correlation (FIDVC; Bar-Kochba *et al.*, 2015; Figure 1B), which tracks local matrix volumes between adjacent time points to generate a map of local matrix deformations around the cell. These 3D, time-lapse data sets allow us to quantitatively relate local matrix displacements to the movement of the cell's cytoskeleton and integrin-based adhesions (Toyjanova *et al.*, 2014).

HFFs embedded in fibrin gels extended large, ~20- to 70-µm protrusions that dynamically deformed the matrix (Figure 1A and Supplemental Video S1). Consistent with previous reports (Petroll and Ma, 2003; Notbohm *et al.*, 2015b), quantification of the matrix displacements revealed motions both toward and away from the cell body, hereafter referred to as retrograde and anterograde displacements, respectively (Figure 1B). To determine whether anterograde displacements corresponded to anterograde cell-generated internal forces, we ablated cellular contractility with a cocktail of Rho-associated kinase, actin, and myosin light chain kinase inhibitors (Figure 2Ai) and recorded the relaxed, reference fibrin configuration (Figure 2Aii). We then used the relaxed matrix configuration to compute the direction and magnitude of the cell-generated matrix deformation immediately before ablation (Figure 2Aiii). To relate local matrix deformations to cell geometry, we reconstructed the cell surface and mapped local matrix deformations onto this surface (Figure 2Aiv) using a procedure described by Stout *et al.* (2016).

Quantification of the resulting matrix deformations confirmed that HFFs at times generated anterograde matrix displacements, which often appeared as a contraction deformation of the matrix (Figure 2B). In some cases, protrusions generated what appeared to be shearing deformations, with retrograde and anterograde deformations on opposite sides of the same protrusion (Supplemental Figure S1).

Because in two dimensions there is a relationship between the actomyosin structure and proximal traction force magnitude (Gardel *et al.*, 2008), we sought to understand how displacement and strain changed as a function of distance from the protrusion tip. To do so, we collapsed displacement and strain values onto an axis extending from the protrusion tip to base (Figure 2C). Across multiple cells, we observed large, multimicrometer matrix deformations close to the protrusion tip, which decayed in magnitude closer to the cell body (Figure 2D; additional examples in Supplemental Figure S2). To better understand the directionality of deformation and its relationship to the cell membrane, we calculated the magnitude of the displacement both perpendicular and tangential to the cell surface (Figure 2, E and F). We found that cells slightly contracted the fibrin inward both along protrusion surfaces (Figure 2E) and around the nucleus (Supplemental Figure S3) but generated much larger tangential displacements aligned parallel or antiparallel with the protrusion axis (Figure 2, F and G).

Matrix strain is better than raw displacement measurements at indicating where the cell applies mechanical force to its environment, because matrix stresses and tractions are proportional to measured matrix strains and the mechanical properties of the ECM. Matrix strain mapped along the protrusion axis showed distinct zones of compression (negative strain) and stretch (positive strain; Figure 2H). Averaged across multiple cells, the fibrin was stretched along the first 14 µm of the protrusion tip and compressed closer to the cell body (Supplemental Figure S2), suggesting that retrograde-oriented cell forces were primarily applied to the matrix tens of micrometers back from the protrusion tip. The presence of multiple stripes of compression and stretch within some protrusions similarly suggested the presence of cell-generated forces in distinct zones that were distant from the protrusion tip.

To summarize, HFFs generated large protrusions when embedded in a soft fibrin matrix that generated matrix displacements that were primarily oriented both retrograde and anterograde relative to the protrusion axis. Of importance, high strains were observed at multiple locations throughout protrusions. These observations are incompatible with a picture in which the cell generates traction stresses largely at the cell edge, as is observed in two dimensions, and instead suggest that traction stresses might be transduced to the matrix at several spatially distinct sites throughout the cell's surface. Motivated by these considerations, we examined the nature of the physical linkage between the cell cytoskeleton, integrin-based adhesions, and the surrounding matrix.

### HFFs embedded in 3D fibrin form stress fibers flanked by focal adhesions

We next imaged the nature of the adhesions linking the HFFs to the surrounding fibrin matrix. To do so, we fixed samples 10 h after cell seeding on fibrin-coated coverslips (two dimensions) or embedded in fibrin (three dimensions) and stained for ECM, FA, and actomyosin cytoskeleton components. Secreted fibronectin was observed surrounding cells embedded in 3D fibrin (Supplemental Figure S4). This situation recapitulates a key feature of provisional matrices in vivo, which consist of a mixture of fibrin

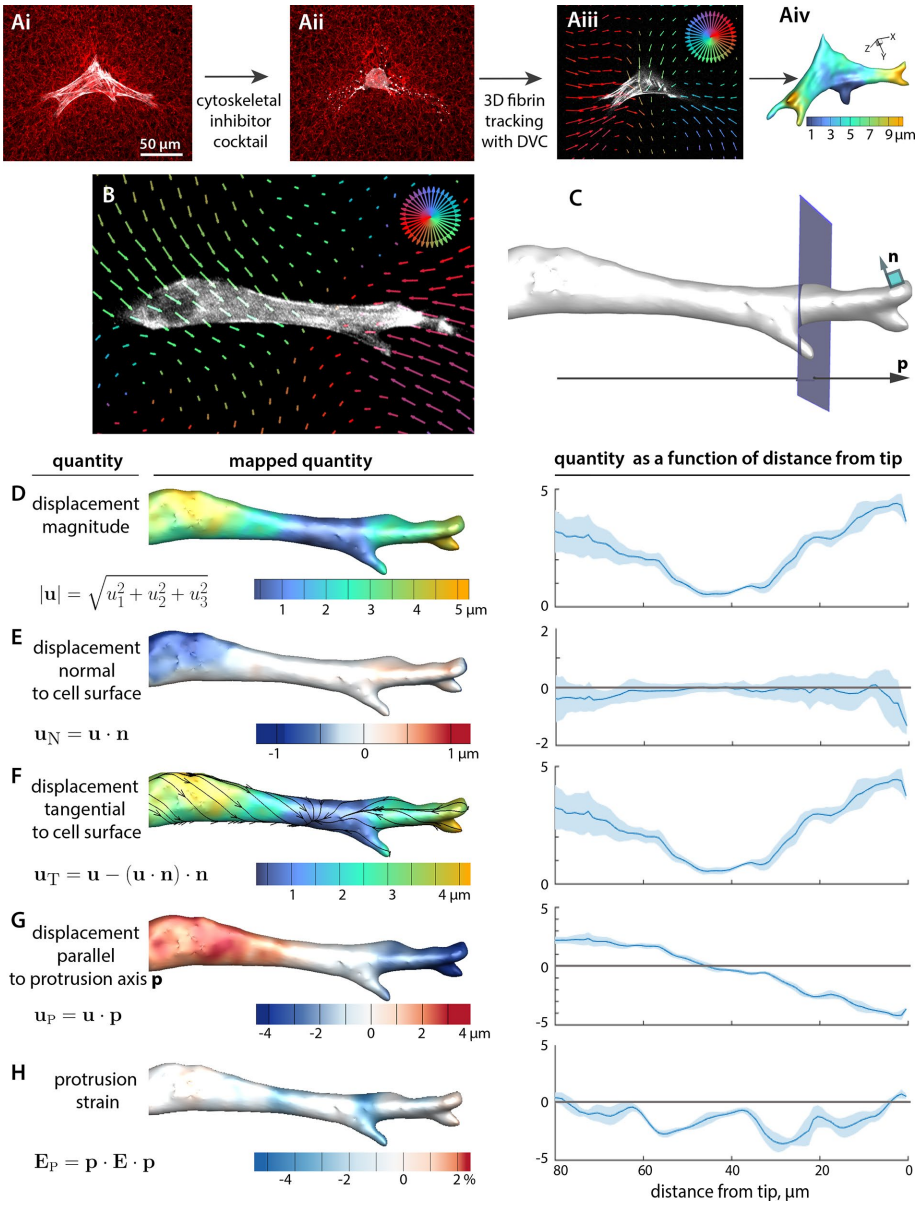


FIGURE 2: Decomposition of cell-induced matrix deformations reveals traction profiles. (A) Fibrin deformations determined relative to a relaxed reference. After imaging a cell expressing EGFP-MRLC embedded in a fibrin gel (i), a relaxed reference fibrin configuration was acquired by treatment of the cell with a cocktail of cytoskeletal inhibitors (ii). Comparison of the fibrin configuration between images i and ii gives the deformation of the fibrin matrix relative to a relaxed state (iii). (iv) Cell-induced fibrin deformation mapped onto the cell surface. (B) Quiver plot of a sample *z*-slice of the fibrin displacement map derived from the experiment in A showing an example of a simultaneous anterograde–retrograde deformation event. (C) 3D reconstruction of the cell in B, showing the protrusion axis, **p**. An example set of points equidistant along **p** is indicated by the purple plane. The axis **p** is defined as the vector from the protrusion tip to the protrusion base, which lies before the nucleus. Points equidistant along **p** are collapsed to generate the profiles in the bottom plots given as a function of distance from tip (median plotted, bounded by 1 SD). More detail can be found in *Materials and Methods*. (D) Magnitude of the matrix displacements for the cell in B. (E) Magnitude of the displacement perpendicular to the cell surface, determined at every point on the cell surface (vector **n** shown in C). Negative values denote inward fibrin deformation, and positive values denote deformation away from the cell surface. (F) Displacement tangential to the cell surface, with the streamlines marking direction. (G) Magnitudes of the anterograde (red) and retrograde (blue) displacement components. (H) The protrusion strain, **p•E•p**, where **E** is the Lagrange strain tensor. Positive values reflect stretch, and negative values reflect compression.

and fibronectin (To and Midwood, 2011). Consistent with the observed matrix strains, we observed large adhesion complexes, hereafter referred to as FAs, across the cell surface (Supplemental Figure S4). The large majority of FAs contained paxillin and $\alpha_5/\alpha_5\beta_1$ integrin (Supplemental Figures S5Biv, 6B, and 7). Of interest, in a subset of cells, $\alpha_v$ integrin also localized selectively to adhesions at protrusion tips (Supplemental Figures S5Biii and 6A). These observations are consistent with analogous measurements for HFFs adhering to fibrin-coated glass (Supplemental Figures S5A and 7) and are also broadly consistent with reports of the adhesion composition for HFFs adhering to 3D, decellularized matrices (Cukierman *et al.*, 2001). The $\alpha_5$ integrin appeared at the termini of phalloidin-positive 3D actin bundles both in protrusions and throughout the cell body (Supplemental Figure S8B). All visible actin bundles were decorated with punctate myosin IIA and, in many but not all cases, punctate α-actinin-1 (Supplemental Figure S8A). These features are consistent with the molecular hallmarks of contractile stress fibers.

## Paxillin plaques exhibit both retrograde and anterograde movements

To gain insight into how cell adhesions are coupled to matrix deformations, we used time-lapse, live-cell imaging to visualize the relative motion of EGFP-paxillin and fibrin. Paxillin plaque velocities were tracked in three dimensions with a particle tracker (the ImageJ plug-in TrackMate), which links the centroids of particles between time points (Tinevez *et al.*, 2016). Because particle tracking can overestimate velocities when the localization error is substantial compared with the true displacement (see Supplemental Discussion, Characterization of localization error contribution to velocity and determination of robust time resolution for velocity reporting), we report paxillin plaque velocities calculated from 10 ± 1–min steps. We find that plaque displacement in this time is sufficient to suppress overestimation of velocity from localization error (Supplemental Discussion and Supplemental Figure S9). We observed that many paxillin plaques were stable on the time scale of imaging (in some cases up to 4 h) and often moved multiple micrometers without disassembling (Figure 3A).

Comparison of the velocities of individual EGFP-paxillin plaques with that of the proximal matrix (tracked with FIDVC)

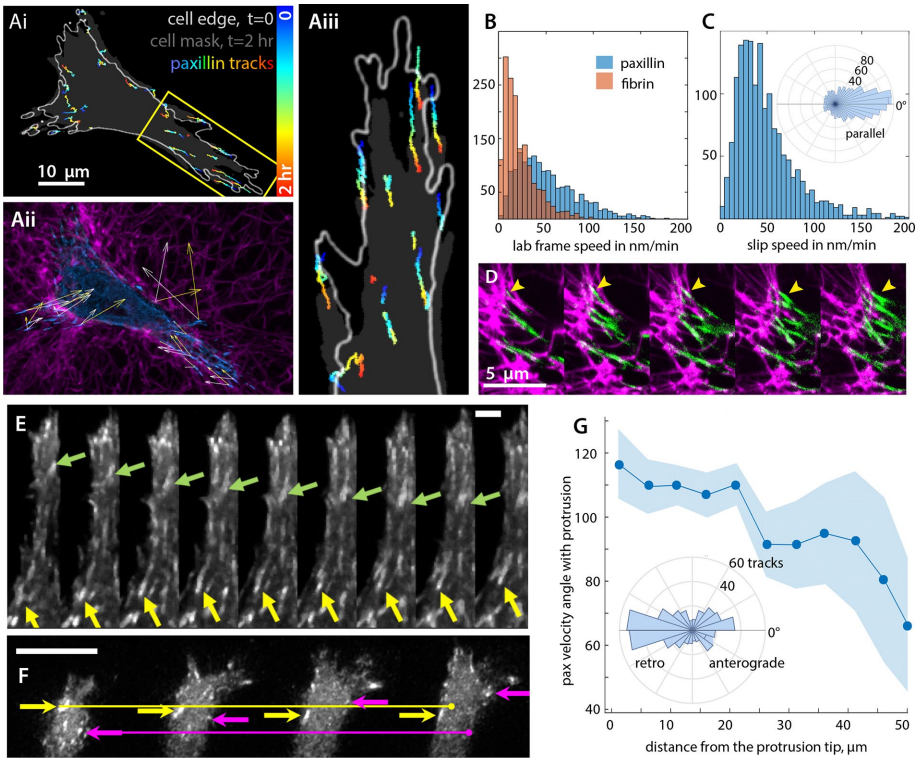


FIGURE 3: Tracking paxillin dynamics reveals that adhesions move both toward and away from the cell body and slip relative to the surrounding matrix. (Ai) Automated 3D particle tracking of EGFP-paxillin plaques. The cell outline at $t = 0$ is shown in white, and the final location of the cell is shown in gray. Rainbow-colored lines indicate the paths of individual paxillin plaques, with blue at $t = 0$ and red at $t = 2$ h. (Aii) Sample $z$-slice for the cell in A, with paxillin in cyan and fibrin in magenta. Instantaneous paxillin velocities for plaques centered in this $z$-slice are shown in yellow, and the fibrin displacement at the corresponding voxels are shown in white. (Aiii) Magnified image of the paxillin plaque tracking in Ai. (B) Quantification of paxillin velocities and that of the fibrin matrix proximal to adhesions from four cells. (C) Difference in velocities, that is, slippage, between paxillin and fibrin. Rose plot inset, angle between the velocity of paxillin and the velocity of the proximal fibrin matrix. (D) Example images of plaques that remain stably adhered to individual fibers over 2 h. Frames are 24 min, 52 s apart. The arrow marks a plaque whose center moves relative to the neighboring ECM. (E) Example of simultaneous retrograde and anterograde movement of EGFP-paxillin plaques. Scale bar = 5 µm. (F) Example of paxillin plaques in close proximity moving in opposite directions. Scale bar = 10 µm (G) Rose plot inset, quantification of the angle between paxillin plaque velocities and the protrusion axis. Angles close to 0° are anterograde, and angles close to 180° are retrograde. Line plot, average angle made by the plaque velocity vector and the protrusion as a function of distance from the protrusion tip. The mean angle of observations within a 5-µm bin is bounded by the 95% confidence interval of the mean. Nine cells.

revealed that paxillin plaques were mechanically coupled to the fibrin matrix, in that they moved in the same direction as fibrin, although at a higher speed (Table 1; 52 ± 2.8 nm/min paxillin mean velocity, 22.8 ± 0.46 nm/min fibrin mean, $p < 10^{-4}$; Figure 3, B and C). Qualitative observations of plaques revealed that this difference in velocity reflected a combination of "slip" relative to the labeled fibrin (Supplemental Video S2) and plaque remodeling (Figure 3D).

Consistent with our matrix deformation measurements (Figure 2G), paxillin plaques exhibited sustained retrograde and anterograde motions along protrusions (Figure 3, E and F), with relatively few motions perpendicular to the protrusion axis (Figure 3G, rose plot inset). In some cases, neighboring adhesions moved at dramatically different velocities or in opposing directions (Figure 3, E and F), suggesting that despite being close in proximity, they were not mechanically coupled. A larger fraction of the plaques at the protrusion tip moved in the retrograde direction than at the protrusion base (Figure 3G), consistent with the predominantly retrograde traction deformations generated at the cellular scale and contraction of the matrix.

### Contractile and locally autonomous stress fibers exert force to drive matrix deformation and cell migration

The retrograde and anterograde movements of the paxillin plaques that we observed suggested that the actomyosin cytoskeleton might undergo similar movements. To visualize the dynamics of the actin cytoskeleton, we labeled F-actin with LifeAct-tagRFP. These data revealed dynamic lengthening and shortening of individual actin bundles (Supplemental Video S3A). To discern whether there was movement within actin bundles, we next examined cells expressing EGFP–α-actinin-1 (Supplemental Video S3B). In many, although not all, cells, EGFP–α-actinin-1 organized into discrete puncta along individual actin bundles that served as fiducial markers for tracking. The bright signal of EGFP–α-actinin-1 spots along actin filaments and the high density of spots across the surface of HFFs enabled long-term (hours) and high-resolution tracking of actin at the surface of HFFs in three dimensions. Similar localization of endogenous α-actinin-1 was observed via immunocytochemistry, indicating that the EGFP–α-actinin-1 likely recapitulated localization of the endogenous protein (Supplemental Figure S8).

Simultaneous visualization and tracking of EGFP–α-actinin-1 puncta and fibrin revealed that the EGFP–α-actinin-1–labeled cytoskeleton moved substantially faster than but approximately parallel to the adjacent fibrin matrix (95.0 ± 0.42 nm/min mean velocity of EGFP–α-actinin-1 and 26.9 ± 0.16 nm/min for fibrin; Figure 4A). As with paxillin, EGFP–α-actinin-1 moved in both the retrograde and anterograde directions along protrusions (Figure 4, B and C, and Supplemental Figure S11) and exhibited the retrograde, contraction, and shearing dynamics (Figure 4C) that were observed in paxillin plaque velocities (Figure 3, E and F) and matrix deformation (Figure 2G and Supplemental Figure S1). Consistent with the myosin IIA recruitment to these bundles, we observed zones in which EGFP–α-actinin-1 puncta contracted together (Figure 4D), suggesting that these bundles both transduced and generated contractile force. Together, these data provide evidence that the actin bundles observed here are functionally equivalent to force-generating stress fibers observed for cells plated on flat, 2D substrates. In addition, these data indicate that individual stress fibers can operate independently of each other within the same protrusion.

The pairwise velocity direction correlation of individual puncta within the same time point revealed that across the cell, the direction of puncta movements tended to be either correlated (the cosine of

| Experiment | Tracked protein | Comments | Mean speed (nm/min) | SE | Time resolution of tracks (min) | Numbers of cells | Number of tracks |
|---|---|---|---|---|---|---|---|
| α-Actinin-1 and paxillin coexpression | Paxillin | | 47 | 1.3 | 10 ± 1 | 4 | 556 |
| α-Actinin-1 and paxillin coexpression | α-Actinin-1 | | 53.0 | 0.3 | 10 ± 1 | 4 | 10,258 |
| α-Actinin-1 and zyxin coexpression | Zyxin | | 55 | 1.5 | 10 ± 1 | 7 | 864 |
| α-Actinin-1 and zyxin coexpression | α-Actinin-1 | | 62.7 | 0.6 | 10 ± 1 | 7 | 3813 |
| α-Actinin-1 and zyxin coexpression | Differential velocity | $\mathbf{v}_{zyx} - \mathbf{v}_{actn}$ (see Supplemental Figure S14, B and E) | 58 | 3.1 | 10 ± 1 | 7 | 192 |
| α-actinin-1 and zyxin co-expression | Differential speed | $\lvert\mathbf{v}_{zyx}\rvert - \lvert\mathbf{v}_{actn}\rvert$ | 29 | 1.8 | 10 ± 1 | 7 | 192 |
| α-Actinin-1 and zyxin coexpression | α-Actinin-1 | Colocalized with zyxin | 58 | 2.8 | 10 ± 1 | 7 | 192 |
| Paxillin tracking with labeled fibrin | Paxillin | | 52 | 2.8 | 10 ± 1 | 4 | 1538 |
| Paxillin tracking with labeled fibrin | Fibrin | Colocalized with paxillin | 22.8 | 0.46 | 10 ± 1 | 4 | 1538 |
| Paxillin tracking with labeled fibrin | Differential velocity | $\mathbf{v}_{fib} - \mathbf{v}_{pax}$ | 49.5 | 0.84 | 10 ± 1 | 4 | 1583 |
| α-Actinin-1 tracking with labeled fibrin | α-Actinin-1 | | 95.0 | 0.42 | 3.4–6 | 4 | 25,288 |
| α-Actinin-1 tracking with labeled fibrin | Fibrin | Colocalized with α-actinin-1 | 26.9 | 0.16 | 3.4–6 | 4 | 25,288 |
| α-Actinin-1, all experiments | α-Actinin-1 | | 63.2 | 0.22 | 10 ± 1 | 21 | 30,272 |
| Paxillin, all experiments | Paxillin | | 53.9 | 0.61 | 10 ± 1 | 12 | 3449 |
| Zyxin, all experiments | Zyxin | | 55 | 1.4 | 10 ± 1 | 7 | 864 |

**TABLE 1:** Mean speeds calculated in all experiments.

the angle between their velocities was close to 1) or anticorrelated (the cosine of the angle between their velocities was close to −1; Figure 4E). Examination of the relationship between the distance between puncta and their directional correlation revealed that correlated motion decayed over ~10 μm (Figure 4F) and reached a local minimum at ~50 μm (Figure 4F and Supplemental Figure S12). This is consistent with the idea that these bundles are contractile dipoles ~50 μm long, about one-half to one-third the total length of the average 3D cell.

Over 4 h, we observed that 8 of 52 cells migrated at an average rate of 15 μm/h, with an additional 20 of 43 cells exhibiting large cell shape rearrangements (*Materials and Methods*). We found that stress fibers and focal adhesions could be maintained in cells as they migrated and that, in many cases, EGFP–α-actinin-1 puncta moved toward the protrusion tip during protrusion extension (Supplemental Figure S13 and Supplemental Video S4). In these cases, protrusion extension appeared to reflect not only actin polymerization at the protrusion tip, but also a forward movement of the already-assembled actomyosin cytoskeleton, a result that contrasts with the commonly observed mechanisms of leading edge extension in two dimensions.

### A dynamic molecular clutch links stress fibers to paxillin-containing adhesions

To gain insight into the nature of the coupling between adhesions and the actin cytoskeleton, we next tracked the relative movement of EGFP–α-actinin-1 puncta and adhesions marked with mCherry-paxillin or tdTomato-paxillin (Figure 5A). Tracking the two proteins simultaneously revealed that in general individual paxillin plaques were less mobile than the α-actinin-1 puncta within the same cell (Figure 5B; 47 ± 1.3 nm/min for paxillin and 53.0 ± 0.3 nm/min for α-actinin-1, $p < 10^{-4}$). A similar difference between focal adhesion speed and actin speed was observed in cells coexpressing adhesions marked with red fluorescent protein (RFP)–zyxin and EGFP–α-actinin-1 (Supplemental Figure S14D; 55 ± 1.5 nm/min for zyxin, 62.7 ± 0.6 nm/min for α-actinin-1, $p < 10^{-4}$). Because stress fibers appeared to be terminated by paxillin plaques in static immunofluorescence images (Supplemental Figure S8), we next examined whether there was correlated motion locally between focal adhesions and colocalized α-actinin-1 spots. We found that EGFP–α-actinin-1 puncta generally moved in the same direction as adjacent paxillin-labeled focal adhesions (Figure 5C). These results suggest that stress fibers and focal adhesions are mechanically linked, with a

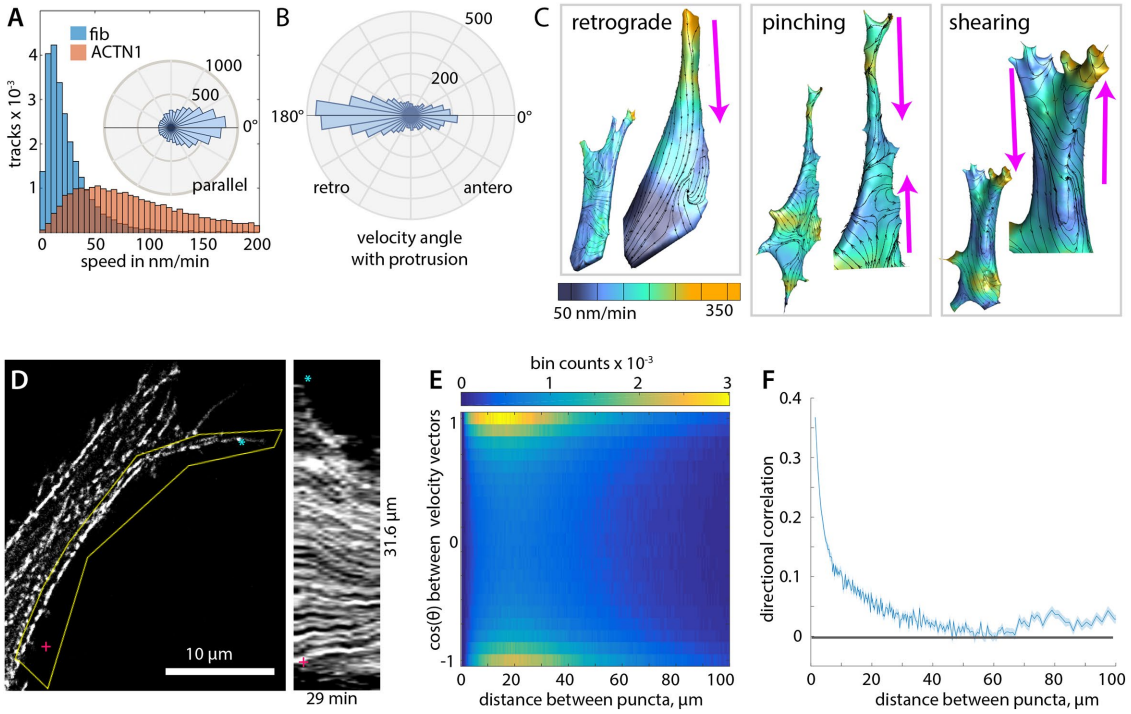


FIGURE 4: Contractile stress fibers operate quasi-independently to contract the local matrix. (A) Distribution of velocities of EGFP–α-actinin-1 and the adjacent fibrin. Rose plot inset, distribution of angles between the EGFP–α-actinin-1 and fibrin velocity vectors for four cells. (B) Distribution of angles between the protrusion axis and EGFP–α-actinin-1 velocity for 25 protrusions in 18 cells. (C) EGFP–α-actinin-1 instantaneous velocity mapped onto the cell surface reveals examples of simultaneous retrograde motion, convergent motion, and shearing motion within protrusions. Here the whole cell depicted for the retrograde case was imaged soon after imaging the zoomed protrusion shown. (D) EGFP–α-actinin-1 in a 3D protrusion that contracts over the course of 29 min. The yellow outline specifies the bounds of the stress fiber that is tracked in the kymograph to the right. Asterisk and red plus sign specify corresponding locations between the image and kymograph. (E) Density map depicting the distance between EGFP–α-actinin-1 puncta and the angle between their velocity vectors. A cos θ = 1 indicates puncta moving in parallel, and cos θ = −1 indicates puncta moving in opposite directions. (F) The median cosine of the angles shown in E as a function of interpunctum distance shows a decay with distance and a local minimum at ~50 µm. Each point is a distance bin containing $10^3$ correlations, and the line is bounded by the SE.

difference in relative velocities that is consistent with the general features of the molecular clutch model.

In many adhesions, EGFP–α-actinin-1 and mCherry/tdTomato-paxillin appeared to move with approximately the same speed and direction, suggesting a stable association. However, for a subset of adhesions, we observed that new EGFP–α-actinin-1 puncta appeared to nucleate at paxillin plaques and flow into existing actin bundles (Figure 5D and Supplemental Video S5). We observed similar results when we labeled focal adhesions with RFP-zyxin (Supplemental Figure S14A). This occurred in plaques both at protrusion tips and in the cell body, both of which could recruit vasodilator-stimulated phosphoprotein (VASP; Supplemental Figure S15), meaning that stress fibers could elongate in both the retrograde and anterograde directions. The addition of new material at the ends of stress fibers was counterbalanced by fiber contraction and, qualitatively, by what appeared to be the convergence and disassembly of individual puncta, thus maintaining a close-to-constant length at short time scales.

To explore further the nature of the physical linkage between stress fibers and their associated adhesions, we quantified the difference in velocities between adhesions marked with RFP-zyxin and proximal EGFP–α-actinin-1 puncta, which, within the limits of our measurement, appeared to be part of stress fibers attached to the adhesion (Supplemental Figure S14). By subtracting the velocity vectors of zyxin plaques from the lab-frame velocity vectors of colocalized EGFP–α-actinin-1 puncta, we find that EGFP–α-actinin-1 puncta flow out of zyxin plaques at a mean rate of 58 ± 3.1 nm/min, with relative velocities ranging from <20 to >180 nm/min (Supplemental Figure S14E). This overall value is in reasonable agreement with the movement of individual EGFP–α-actinin-1 puncta relative to nearby adhesions as tracked by hand (Supplemental Figure S14A and, Figure 5D). The broad distribution of relative velocities likely reflects a range of mechanical connections between stress fibers and actin, ranging from stable associations with negligible slippage to those in which new actin filaments are actively incorporated into the stress fiber (Supplemental Video S5).

In summary, tracking individual adhesions and their associated stress fibers revealed the nature of their physical association. In many cases, the adhesion and the associated stress fiber moved in tandem, with negligible differences in velocity. However, for a subset of adhesions, we observed a differential velocity of EGFP–α-actinin-1 puncta relative to their associated adhesions, consistent with the addition of new material to the stress fiber at its point of attachment. The latter behavior is generally consistent with the molecular clutch model, in that it generates a difference in relative velocities between adhesions and the actin cytoskeleton.

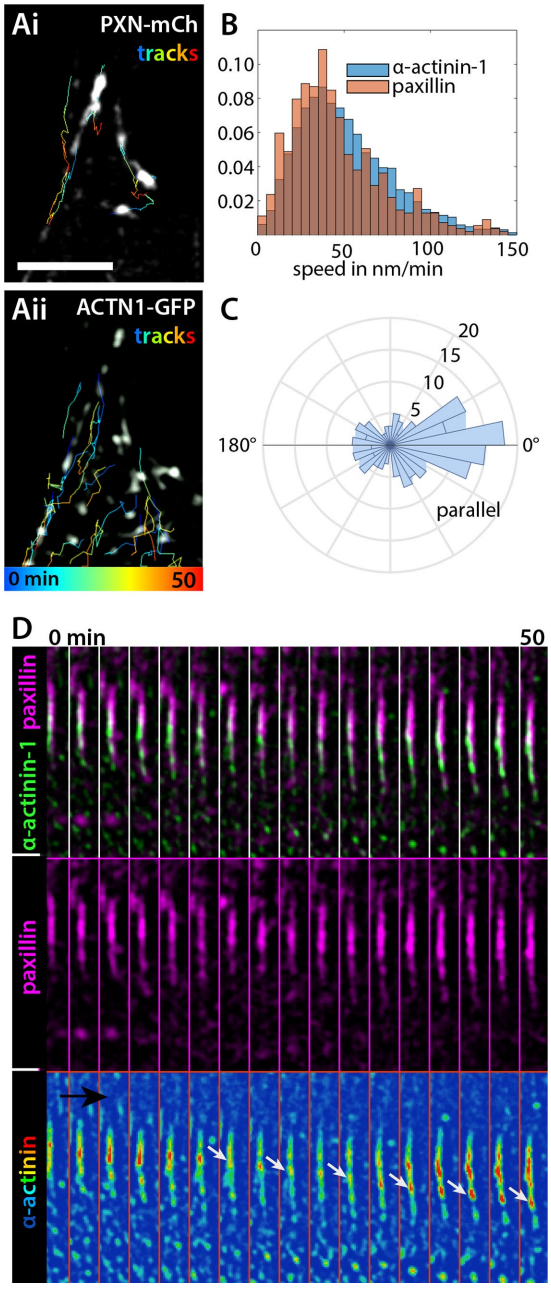


FIGURE 5: α-Actinin-1 bundles elongate from paxillin plaques. (A) Simultaneous imaging and tracking of paxillin (i) and α-actinin-1 (ii), colored to indicate positions from 0 (blue) to 50 (red) min. Scale bar = 5 μm. (B) Distribution of speeds for paxillin plaques and EGFP–α-actinin-1 puncta colocalized with those plaques. (C) Distribution of angles between paxillin and colocalized EGFP–α-actinin-1 velocities. Four cells. (D) Close examination revealed that EGFP–α-actinin-1 puncta nucleated and flowed out of a subset of paxillin plaques. White arrows highlight an EGFP–α-actinin-1 spot that is nucleated within the focal adhesion and flows into the stress fiber. Black arrow: Note the lack of EGFP–α-actinin-1 above the focal adhesion. Panel height, 13 μm.

### Physical models can quantitatively account for cytoskeletal architecture and dynamics

We were intrigued that the fibroblasts used here showed hallmarks of cells cultured on stiff substrates, even though the bulk Young's modulus of the fibrin matrix was only ~200 and ~300 Pa without and with cells, respectively (Supplemental Figure S10). To understand how a mechanically soft environment could potentially engender this response, we performed a mechanical simulation of a model fibrin matrix constructed of a 2D fiber network (Abhilash *et al.*, 2014; Notbohm *et al.* 2015a). In these simulations, a point load was applied to a node in a randomly generated matrix to simulate the force exerted by an isolated adhesion (Figure 6A). We then computed force versus displacement curves for multiple random network configurations (Figure 6B). We observed a wide variation in effective stiffnesses, with an average effective force constant of up to ~24 nN/μm for some nodes. These stiffnesses correspond to effective Young's moduli of ~50 kPa (Supplemental Discussion), sufficient to trigger the cellular response to a "stiff" environment. The basic result—that a subset of nodes can provide appreciable local stiffnesses—is robust to assumptions concerning fibrin material properties (Supplemental Figure S16).

Some care is required in interpreting the absolute magnitudes of the effective stiffnesses inferred from this simulation. It is plausible that a fully 3D matrix would be softer than the 2D model used here due to the presence of additional, soft bending modes. Conversely, the model does not account for the effect of force generated by multiple cellular adhesions or the proximity to the coverslip surface (in some cases approaching ~1 μm due to the working distance of the objective), which may increase the effective stiffness experienced by the cell. Nevertheless, the model is useful in showing that 1) nodes within a model fibrin matrix may differ in effective stiffnesses by an order of magnitude, and 2) reasonable bulk material properties result in effective, local stiffnesses that can plausibly support stable adhesion formation.

We next sought to understand how physically stable connections between the actin cytoskeleton and the ECM might arise in our system. In particular, we sought a model that could recapitulate the rate of slippage of α-actinin-1 relative to adhesions, which, as noted, ranged from negligible to >180 nm/min. Inspired by earlier theoretical work (Schwarz *et al.*, 2006; Chan and Odde, 2008; Novikova and Storm, 2013), we sought to develop a minimalist, analytical model of the connections between the ECM, adhesion, and cytoskeleton (Supplemental Discussion). To do so, we treated the physical linkage between the focal adhesion and actin cytoskeleton as existing in a state of mechanical and compositional pseudoequilibrium. This approach resulted in readily interpretable analytical expressions that describe actin velocity as a function of the mechanical load. In particular, for large adhesions the actin velocity, $v$, is given by

$$v = \frac{F_{\text{tot}}\left(k_{\text{on}} + k_0\right)}{\kappa\left(k_{\text{on}}C_t - \alpha_c F_{\text{tot}}\right)}\left[k_0 + \frac{\alpha_c F_{\text{tot}}\left(k_{\text{on}} + k_0\right)}{\left(k_{\text{on}}C_t - \alpha_c F_{\text{tot}}\right)}\right]$$

Here $v$ is a function of the total force ($F_{\text{tot}}$) and number of mechanical linkages (clutches; $C_t$) present in the adhesion, the kinetic rate constants at zero load for actin binding and release by the adhesion "clutch" ($k_{\text{on}}$ and $k_0$), an effective stiffness experienced by the adhesion (κ), and $\alpha_c$, which parameterizes the force sensitivity of the adhesion–actin linkage (Supplemental Discussion). A negative $\alpha_c$, which describes a catch–bond interaction, results in a clutch dissociation rate that decreases with increasing load. Reasonable parameter values yield values of $v$ consistent with the range of velocities of EGFP–α-actinin-1 relative to zyxin-marked adhesions (Supplemental Discussion). In addition, the model predicts that adhesions that can reinforce in response to applied load (negative $\alpha_c$) will exhibit actin velocities approaching zero (Supplemental Figure S17), in line with our experimental

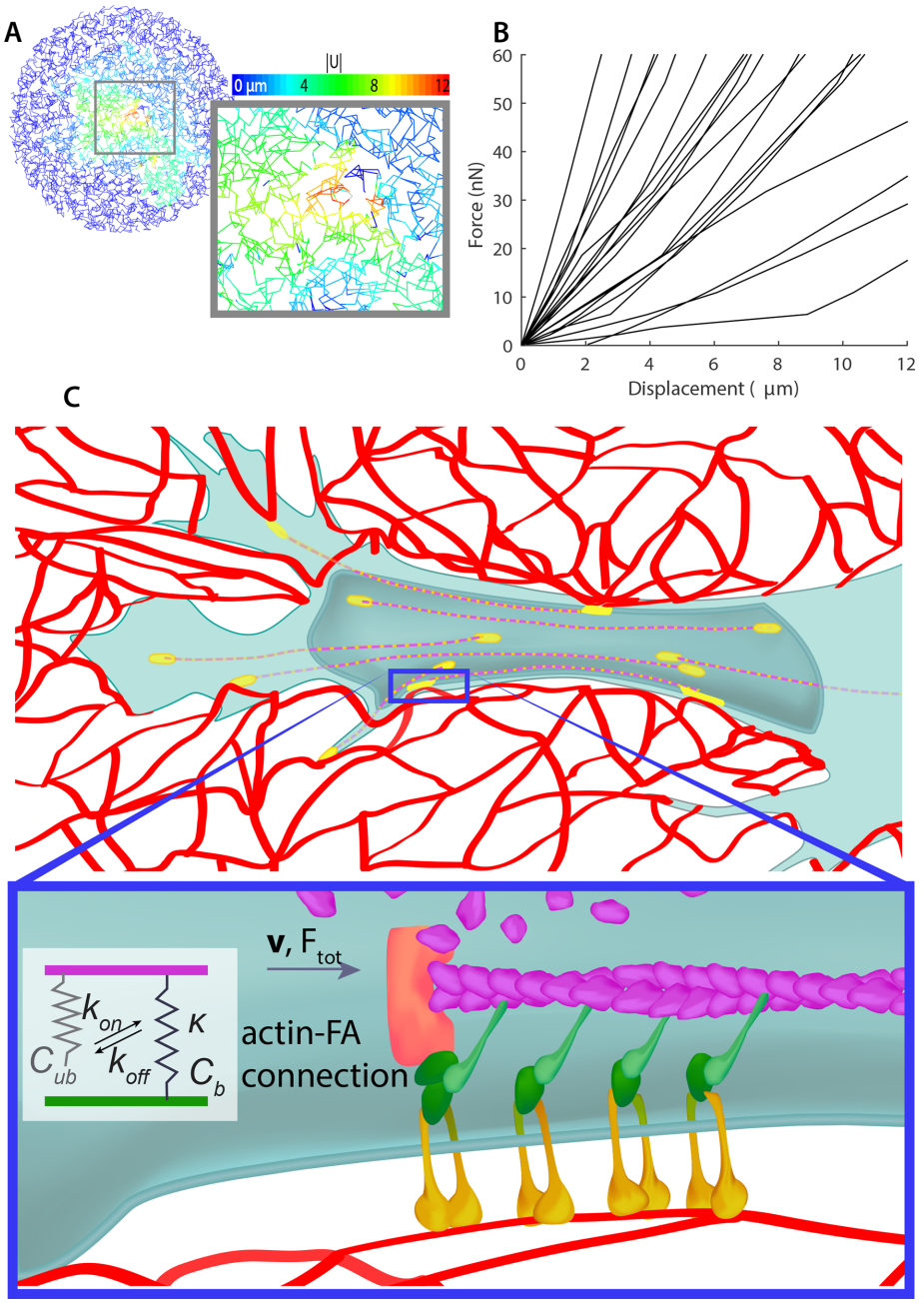


FIGURE 6: Simulations predict adhesion stability under load. (A) Model of a point load applied to a model ECM network shows the propagation of displacement. (B) Force–displacement curves from multiple random networks show high effective stiffnesses at a subset of ECM network nodes, along with strain stiffening in some cases. See Supplemental Figure S16 for a model using alternative stiffness parameters. (C) Model of force transmission between the substrate, focal adhesions, and actin in three dimensions. Yellow, integrins; dark green, paxillin; light green, FA–actin linker proteins; magenta, actin; orange, actin polymerization protein (VASP); red, fibrin. See *Discussion* for details.

observation that many stress fibers are stably attached to the adhesions at their termini.

## DISCUSSION

Here we present a quantitative analysis of how cells transduce cytoskeletal force to the ECM in a soft, 3D environment. The fibrin matrix used here has a bulk elastic modulus that is ~$10^{-7}$ that of glass or plastic and differs fundamentally from flat, continuous surfaces in that it is both porous and confining. Despite these profound differences in material properties, we found that many cells exhibited features that are commonly observed in cells adhering to hard, flat substrates, notably the formation of stress fibers and prominent integrin-based adhesions.

Our study is not the first to examine cellular adhesion, matrix deformation, and cytoskeletal dynamics in 3D environments. Both integrin-based adhesions and bundled actin structures have been observed and tracked in 3D gels, including fibrin (Hakkinen *et al.*, 2011; Kubow and Horwitz, 2011; Doyle and Yamada, 2016). Parallel studies have quantified matrix deformations using a variety of techniques (Bloom *et al.*, 2008; Starke *et al.*, 2013; Notbohm *et al.*, 2015b). In cases in which the material properties of the matrix could be measured or inferred, these deformations could be converted into stresses (Legant *et al.*, 2010; Koch *et al.*, 2012; Steinwachs *et al.*, 2016). However, to our knowledge, no study simultaneously quantified matrix deformation, adhesion, and actin cytoskeletal dynamics in a single cell type under the same conditions in order to explore systematically how mechanical deformations are transduced (Table 1). So far as we are aware, this study is also the first to directly quantify relative velocities of actin and adjacent adhesions, a defining aspect of the molecular clutch model. The data reported here thus complement and extend previous studies by revealing a probable mechanism by which movement in the cell cytoskeleton is coupled to matrix deformations for cells in 3D environments.

Our measured actin speeds are comparable to some reported actin speeds measured in the cell body and lamellum for cells adhering to glass (Ponti *et al.*, 2004; Brown *et al.*, 2006; Gardel *et al.*, 2008) but slower than other measurements of 2D stress fiber elongation at FAs (Hotulainen and Lappalainen, 2006; Wu *et al.*, 2017). In particular, a recent report of tension-dependent stress fiber elongation rates of ~23 (high tension) and ~250 (low tension) nm/min puts our measured speeds within the range of speeds measured for cells on stiff substrates in two dimensions (Tojkander *et al.*, 2015). Considerably faster actin velocities were reported under other circumstances. These include 1 µm/min actin flow speeds within the 2D lamellipodium (Hu *et al.*, 2007) and at the tips of protrusions for cells cultured in 3D matrices (Chiu *et al.*, 2013). Even faster, 5–20 µm/min actin velocities were measured at the periphery of cells adhering to soft substrates (Chan and Odde, 2008; Elosegui-Artola *et al.*, 2016) and near the immunological synapse of cytotoxic T-lymphocytes (Ritter *et al.*, 2015). This wide range in apparent actin velocities is consistent with variants of the molecular clutch model in which actin velocity is set

by the balance of cytoskeletally generated force and drag on actin generated by mechanical linkages to cellular adhesions (Bangasser *et al.*, 2013; Mekhdjian *et al.*, 2017). Low velocities, such as we observe, may reflect a situation in which a relatively large number of mechanical clutches between actin and cellular adhesions overwhelm the contractile forces generated by myosin, resulting in close-to-stalled actin motion.

It is important to note that our measurements report on the motion of α-actinin-1 puncta, imaged within the time resolution limits of our confocal microscopy setup. It is possible that other actin structures present in these cells may undergo dynamics distinct from those described here, such as the fast flow within a few micrometers of protrusion tips. However, we do note that that α-actinin-1 colocalized with the large majority of the phalloidin-labeled actin in the cells analyzed. We therefore infer that the dynamics of α-actinin-1 faithfully recapitulate the dynamics of a major portion of the actin cytoskeleton on the time scale that is experimentally accessible.

Previous studies reported that, at least under some circumstances, cells can form prominent actin bundles in 3D extracellular matrix networks (Grinnell and Petroll, 2010) whose relative orientation and attachment to adhesions resemble the noncontractile dorsal stress fibers of cells on glass. However, whether these structures generated contractile stress was unclear. We extend these results by showing that ostensibly similar actin bundles in our study 1) are contractile and contain both nonmuscle myosin II and α-actinin-1, 2) are attached to the matrix at distinct points throughout the length of the protrusion, and 3) undergo movements that are highly correlated with local matrix deformation. In total, these observations suggest that stress fibers can play an important role in traction stress generation in a soft, 3D matrix. Note that our data do not preclude the presence of other force-generating mechanisms. We and others have observed individual cells that could deform the matrix despite the lack of α-actinin-1 recruitment to actin bundles, and multiple mechanisms of force generation, for example, via filopodial extensions (Starke *et al.*, 2013; Kim *et al.*, 2015), have been proposed for fibroblasts and other cell types in mechanically similar environments (Charras and Paluch, 2008; Petrie *et al.*, 2014). Transient lamellipodial dynamics are visible in the protrusion tips of some of our cells and were observed in previous studies (Ritter *et al.*, 2015). As suggested by others (Ritter *et al.*, 2015), actin polymerization at protrusion tips may plausibly generate local forces that contribute to nascent adhesion stabilization and leading-edge protrusion but are not directly observable here due to limitations in temporal and spatial resolution.

The large matrix deformations, stable adhesions, and contractile stress fibers observed here contrast with the typical behavior of cells on comparably soft 2D synthetic hydrogels. Our model suggests that individual nodes within the matrix may provide locally stiff resistance to deformation sufficient for adhesion maturation and stress fiber formation. Consistent with experimental measurements (Winer *et al.*, 2009; Jansen *et al.*, 2013), our simulations predict some degree of strain stiffening of the network, as can be seen in the increase in slope of some of the force–displacement curves (Figure 6B). We suggest that, in an inhomogeneous, fibrous system, cells respond not so much to the bulk material properties of their surroundings as to the ability of localized regions within the matrix to bear mechanical load. Although other effects—for example, confinement (Pathak and Kumar, 2012; Toyjanova *et al.*, 2015), ECM remodeling/ligand clustering (Baker *et al.*, 2015; Chaudhuri *et al.*, 2015), signaling from soluble factors (Tamariz and Grinnell, 2002), and strain stiffening (Duong *et al.*, 2009; Winer *et al.*, 2009; Jansen *et al.*, 2013)—must also be considered, this explanation is consistent with the data reported here and in other studies examining the response of cells to plastically deformable, 3D matrix environments (Mochitate *et al.*, 1991; Tomasek *et al.*, 1992; Grinnell, 1994; Tamariz and Grinnell; 2002; Grinnell and Petroll 2010).

Quantification of cytoskeletal, adhesion, and matrix dynamics supports a mechanistic explanation for how fibroblasts generate and exert traction stresses in the context of a fully 3D environment. We observed continuous slippage between α-actinin-1, paxillin-labeled adhesions, and fibrin. However, this slippage did not reflect continuous retrograde cytoskeletal flow, as is often the case for cells adhering to flat surfaces. Instead, our data are consistent with a model in which each adhesion possesses a cytoskeletal clutch that operates semiautonomously by the continuous elongation of stress fibers, plausibly mediated by VASP (Tojkander *et al.*, 2015) or formins (Hotulainen and Lappalainen, 2006; Khatau *et al.*, 2012; Oakes *et al.*, 2012; Skau *et al.*, 2015; Tee *et al.*, 2015; Wu *et al.*, 2017) at their anchorage points. Previous high-resolution traction force measurements were similarly interpreted to imply that neighboring adhesions operated autonomously (Plotnikov *et al.*, 2012). Our study extends this observation to a 3D environment and in addition reveals its biological usefulness in a discontinuous matrix.

The mechanisms of adhesion and traction force generation described here may be directly related to the physiological role of fibroblasts in wound contraction and ECM remodeling after injury. We observed that stress fibers within protrusions operated semiautonomously, such that each adhesion can maintain tension on the matrix even as the cell migrates through and remodels the provisional matrix. The dynamic mechanical equilibrium that we observe is also consistent with protrusion extension: in some cells, we observed that the extension of a subset of stress fibers was coincident with coordinated anterograde movement of the cytoskeleton and protrusion extension. This mechanism of protrusion extension likely coexists with actin polymerization at protrusion tips, analogous to that observed in the lamellipodium of cells cultured in two dimensions. The stress fiber–based mechanism of force generation (Figure 6C) that we observe may thus allow fibroblasts to maintain consistent attachments to the matrix and matrix contraction as they migrate through and remodel the ECM, a picture that is consistent with their physiological function.

## MATERIALS AND METHODS

### Cell culture

HFFs (also known as human dermal fibroblasts) were acquired from the American Type Culture Collection (CRL-02091) and cultured in 4.5 mg/ml glucose DMEM (21063-029; Life Technologies) supplemented with 10% fetal bovine serum (FBS; Corning) and 1× sodium pyruvate (Life Technologies). HFFs stably expressing EGFP-paxillin were prepared using the PiggyBac system (Transposagen Biopharmaceuticals) and were cultured identically to untransformed HFFs. HFFs stably expressing EGFP-MRLC1 in the PiggyBac backbone were prepared similarly to the EGFP-paxillin HFFs. HFFs were used between passages 5 and 12 for experiments. Mycoplasma testing was performed approximately every 3 mo.

### Transfection and constructs

HFF transfections were performed with the Lonza 4DX Nucleofector using the P2 Primary Cell Solution kit (PBP2-02250) and the NHDF transfection protocol. Transfections were performed with 1–1.5 μg of pEGFP–N1-α-actinin-1 (a gift from Carol Otey, University of North Carolina, Chapel Hill; Addgene plasmid 11908), 1 μg of pCMV-Life-Act-TagRFP (purchased from Ibidi), 1.4 μg of tdTomato–paxillin-22 (a gift from Michael Davidson, National High Magnetic Field Laboratory

and Department of Biological Science, Florida State University; deceased 2015; Addgene 58123), pEGFP-MRLC1 (a gift from Tom Egelhoff, Lerner Research Institute, Cleveland Clinic; Addgene 35680[1]), and/or RFP-zyxin (a gift from Anna Huttenlocher, University of Wisconsin–Madison; Addgene plasmid 26720; Bhatt *et al.*, 2002).

### Fibrin gel sample preparation

Unlabeled fibrinogen (from human plasma, >95% clottable) was purchased from VWR (80051-620), and stocks of 15 mg/ml were made by dissolving lyophilized fibrinogen in 1× Hanks balanced salt solution (HBSS). Then 500-µl aliquots were flash frozen and stored at –80°C.

Fibrinogen was fluorescently labeled with Alexa Fluor 647 NHS Ester (succinimidyl ester; ThermoFisher). Lyophilized fibrinogen was resuspended in 100 mM sodium borate, pH 8.2, at a concentration of 15 mg/ml. Alexa 647 dye was solubilized in dimethyl sulfoxide (DMSO; 472301; Sigma-Aldrich) at a concentration of 100 mM. The dye was added to the fibrinogen at a ratio of 10:1 (dye:fibrinogen) and incubated on a shaker at room temperature for 1 h and 4°C for 1 h. The labeled protein was dialyzed extensively in HBSS at 4°C over 2 d to remove excess fluorophore, resulting in a final concentration of 6 mg/ml. Thrombin from human plasma (T1063; Sigma-Aldrich) was solubilized to 100 U/ml in HBSS and stored at –80°C.

The 2.25 mg/ml fibrin gels (with 10% FBS) were prepared by mixing 375 µl of labeled (6 mg/ml) or 150 µl of unlabeled (15 mg/ml) stock fibrinogen solution with HBSS to a volume of 800 µl and degassing in vacuum for 15 min. We added 100 µl of cells suspended in cell culture medium at a density of $(0.5–5) \times 10^5$ cells/ml (with the exception of the experiment in Supplemental Figure S13 and Supplemental Video S4, which diluted a volume of $1 \times 10^6$ cells/ml) and 100 µl of FBS to the fibrinogen mixture. One unit of thrombin was added to the mixture, pipetted three times to mix, and immediately transferred to a LabTek imaging dish for polymerization for 1 min at room temperature followed by 15 min at 37°C. Samples prepared for fixation were added to the coverslip in small volumes after thrombin addition (~20 µl) and turned upside down after the 1-min room temperature polymerization step to prevent the cells from settling to the bottom coverslip during polymerization. After 15 min of polymerization at 37°C, cell culture medium was added on top of gels. Cells spread in gels for 8–20 h (depending on experiment) before fixation or imaging.

### Fibrin-coated coverslip preparation

Fibrin-coated coverslip experiments were performed with Alexa 647–labeled fibrinogen to ensure that the cells chosen for analysis had not proteolyzed through the fibrin to the underlying coverslip. Briefly, 30 µl of labeled fibrinogen aliquot was mixed with 2.4 ml of HBSS, 300 µl of cell culture medium, and 300 µl of FBS. One unit of thrombin was added, pipetted to mix, and added to coverslips for polymerization at 37°C for 30 min. The remaining gel was aspirated, and the coverslip was washed once with phosphate-buffered saline (PBS).

### Live-cell imaging

Time-lapse *z*-stacks were acquired on a Zeiss LSM 710 (Figures 1, 2, and 4) or a Zeiss 780 (Figures 3–5) laser scanning confocal microscope using a 63× oil immersion objective (PLAN APO 1.4 numerical aperture). All experiments were performed in a humidified, thermally controlled chamber at 37°C in the presence of 5% $CO_2$. HFFs in Supplemental Figure S2 and S4–S6 were imaged 15–20, 8–12, 10–14 , or 12–14 h, respectively, after gel preparation. The fibrin gel was imaged via the fluorescence of the conjugated Alexa 647 fluorophore (see *Fibrin-coated coverslip preparation*).

### Fibrin relaxation experiments

HFFs expressing EGFP-MRLC were embedded in fibrin gels and allowed to spread for 15–20 h. A single *z*-stack of the EGFP and fibrin signals was taken for each cell, and a cocktail of cytoskeletal inhibitors (minimal final concentrations of 20 µM Y27632, 40 µM ML-7, and 20 µM of latrunculin A) was added to ablate cell contractility. After a 1- to 2-h incubation with the drug cocktail, the resulting fibrin configuration and cell signal were imaged. The *z*-stacks from the intact cell and relaxed cell were registered against the fibrin signal, and the resulting displacement of fibrin between these two images was used in Figure 2.

### Immunofluorescence labeling

HFFs in gels were fixed with 4% paraformaldehyde (Polysciences) for 15 min and washed twice with PBS, followed by two 5-min washes in PBS at room temperature. Samples were permeabilized with 0.1% Triton X-100 for 5 min, blocked with 5% bovine serum albumin (BSA) for 2 h at room temperature or overnight at 4°C, and subsequently incubated with primary antibody at a dilution of 1:100 in 1% BSA for 4 h at room temperature or overnight at 4°C. Cells were then washed twice with PBS, followed by two 5-min washes in PBS and a 1-h wash at room temperature. Secondary antibody at a dilution of 1:100 was applied for 2 h at room temperature. Samples were washed twice with PBS, followed by two 5-min washes in PBS and 30 min PBS at room temperature. When noted, a fluorescently labeled phalloidin was applied for 10 min at room temperature following the manufacturer's instructions and washed twice in PBS, followed by two 5-min washes in PBS.

Rabbit anti–$\alpha_5$ integrin (ab150361), mouse anti–α-actinin-1 (ab11008), Alexa 488–conjugated anti-mouse secondary antibody (ab150117), and Alexa 405–conjugated anti-rabbit secondary antibody (ab175649) were purchased from Abcam. Mouse primary antibodies raised against $\alpha_5\beta_1$ integrin (MAB1999), $\alpha_v\beta_3$ integrin (MAB1976), and paxillin (05-417) were purchased from Millipore. Mouse anti–$\alpha_v$ integrin (ALX-803-304-C100) antibody was purchased from Enzo Life Sciences. Rabbit anti-MYH9 (nonmuscle myosin heavy chain IIA, PRB-440P) antibody was purchased from Covance. Phalloidin (ActinRed 555 ReadyProbes; R37112) was purchased from ThermoFisher.

### Fibrin characterization

We cast 1-ml gels in the inner well (14 mm diameter) of 35-mm MatTek coverslip cell culture dishes (P35G-1.5-14 C) as described earlier. Storage and loss moduli were determined using an 8- mm crosshatch probe on an ARES-G2 rheometer (TA Instruments) in a frequency sweep at 5% strain and at 37°C. Experiments were performed at the Soft and Hybrid Materials Facility in the Stanford Nano Shared Facilities. The reported Young's modulus was computed from the shear modulus assuming a Poisson ratio of 0.5.

### Five-dimensional (3D + time + multicolor) preprocessing

Data were registered with the ImageJ Correct 3D Drift plug-in against the fibrin channel, followed by correction for photobleaching with the Bleach Correction (histogram-matching method) option.

### Fibrin tracking with DVC

The FIDVC (Bar-Kochba *et al.*, 2015) algorithm implemented in MATLAB was used to calculate 3D displacements between the input volume images. FIDVC correlated the spatially varying fluorescence intensity produced by the fluorescently labeled fibrin in the input volumes to compute displacements. For FIDVC, the initial subset voxel size was $128 \times 128 \times 64$, with final subset spacing of 8 voxels.

### DVC output registration for relaxation experiments

The output from DVC is a set of three 3D matrices (**u1**, **u2**, **u3**), each mapping in three dimensions the displacement between the input volume images (Bar-Kochba *et al.*, 2015). The data were registered in the *xy*-plane by subtracting median(**u1**) from **u1** and median(**u2**) from **u2**. A triangulated cell surface was generated from the EGFP signal (see *Cell surface rendering*). The **u3** component of displacement was interpolated to the coordinates of the vertices of the cell surface, and the mean value of these *z*-displacement values was subtracted from the map of **u3**. We chose this strategy to minimize the displacement in the *z*-axis at the cell surface because the relaxation of the gel is not symmetric in *z*, possibly because of physical anisotropies resulting from the presence of the coverslip.

### Fibrin strain calculation

In continuum mechanics, the displacement vector, $u_i$, connects the material point $X_i$ in the reference configuration to the deformed configuration, $x_i$, through

$$x_i = X_i + u_i \tag{1}$$

Note that all formulas here follow Einstein notation. This equation can be differentiated to obtain the deformation gradient, $\boldsymbol{F}_{ij}$. The displacements are provided by the results from the FIDVC algorithm:

$$\boldsymbol{F}_{ij} = \delta_{ij} + \frac{\partial u_i}{\partial X_j} \tag{2}$$

Here $\delta_{ij}$ is the Kronecker delta operator. The gradients were calculated numerically using the optimal-9 tab filter, described in detail by Farid and Simoncelli (2004).

The Lagrange strain was calculated as

$$E_{ij} = \frac{1}{2}\left( \frac{\partial u_i}{\partial X_j} + \frac{\partial u_i}{\partial X_i} + \frac{\partial u_k}{\partial X_i}\frac{\partial u_k}{\partial X_j} \right) \tag{3}$$

The protrusion-axis strain (Supplemental Figure S2) was determined with respect to **P**, the vector pointing from protrusion base to tip (described in *Fibrin displacement decomposition*). A change of basis was performed on the deformation gradient tensor such that the first component is parallel to the protrusion axis, with positive values corresponding to stretch along the protrusion axis and the negative values corresponding to compression along the protrusion axis, and this first component is reported in Supplemental Figure S2.

### Fibrin displacement decomposition

The protrusion-axis displacement (Figure 2G) was determined as follows. The voxel locations of the protrusion tip and protrusion base were determined manually, and their coordinates were entered into MATLAB. The protrusion axis, **p**, was determined to be the vector from base to tip.

The parallel component of displacement along the protrusion axis (Figure 2G) was computed from the dot product between **p** and the displacement vector at each voxel,

$$u_p^u = u \bullet \hat{p} \tag{4}$$

The DVC output and each strain scalar were interpolated via a cubic interpolation to match the voxels in the raw image. The displacements normal and tangential to the cell surface were determined from the cell-triangulated surface generated in *Cell surface rendering*.

### Cell surface rendering

The cell surface was determined from the binary mask of EGFP-MRLC intensity (Figure 2) or EGFP–α-actinin-1 intensity (Figure 5). Masks from EGFP-MRLC were as follows. The image was filtered by running a $3 \times 3$ median filter kernel thrice through each *z*-slice of the input volume. Through visual inspection, an appropriate threshold level was selected to obtain a binary image of the cell surface. The cell was determined to be the largest connected volume of the mask. Then gaps and holes in the cell surface binary mask were filled. The triangulation of the cell surface was obtained by running MATLAB's isosurface function on the cell surface binary mask. Laplacian smoothing based on umbrella weights was performed to reduce the noise in the resulting triangulation mesh of the cell surface (Desbrun *et al.*, 1999).

Masks from EGFP–α-actinin-1 intensity were generated as follows: The background was subtracted, the image was median filtered with a 2D kernel that gave a smooth image but retained features (between $2 \times 2$ and $4 \times 4$ pixels), and a binary mask of every *z*-slice was determined with the triangle method in ImageJ. Masks were checked for accuracy and imported into MATLAB, where surface triangulation and smoothing were performed as reported.

### Distance-from-tip cross-sectional analysis and representation

Plots in Supplemental Figure S2 were determined as follows. The protrusion axis, **p**, was determined (as described in *Fibrin displacement decomposition*). Vertex coordinates from the cell surface rendering were assigned to 1-μm bins by distance along axis **p**, and the bin average was determined and plotted as a function of distance along **p**. Thus each point in the plot represents the average value within a 1-μm-thick cross section orthogonal to **p**. Line bounds represent 1 SD from the mean.

### Fiber network simulations

Deformations of a fibrous network were simulated using the finite element software Abaqus 6.12. The typical fiber width and length were estimated from fluorescently labeled images captured with a confocal microscope. Fiber width was estimated from confocal images of fluorescently labeled fibrin; kymographs perpendicular to select fibers were manually generated and fit to a model of square waves of varying widths convolved with the microscope's optical transfer function. The typical width was found to be ~320 nm, and it was assumed that fibers had a circular cross section. Fiber length was estimated for fibers that appeared to start and end in the same imaging plane. Lines were drawn along such fibers, and the length was measured to be ~10 μm. Note that each fiber typically connected to multiple fibers along its 10-μm length, which is accounted for in the model.

The network was generated using a modified lattice-based procedure. Lattice points were generated in a circular region, and randomness was generated as described previously (Notbohm *et al.*, 2015a). Each lattice point formed one endpoint of a fiber. Each fiber's orientation was chosen by picking an angle from a uniformly random distribution, and its length was chosen by picking from a uniformly random distribution between 2.8 and 3.4 times the average lattice spacing. All intersections between fibers were identified; fibers sharing an intersecting point were given a node at that point, and intersecting nodes were pinned together. Nodes on the perimeter of the circular domain were pinned.

Dangling ends and short elements (having length <0.1 times the average lattice spacing) were removed. Elements were simulated as linear beams, each resisting axial tension/compression and bending. The stiffness of these elements can be expressed as a single dimensionless ratio $\kappa = \kappa_b/(\kappa_s l^2)$, where $\kappa_b$ is the resistance to bending, $\kappa_s$ is the resistance to stretching/compressing (equal to Young's modulus times fiber cross-sectional area), and $l$ is the average distance between cross-links (Head *et al.*, 2003; Onck *et al.*, 2005). We estimate a lower bound on $\kappa_b$ from the persistence length, which has been reported for fibrin to be ~40 µm (Piechocka *et al.*, 2010), and $\kappa_s$ from a reported Young's modulus of ~15 MPa for fibers formed in the presence of Factor XIII (Collet *et al.*, 2005) and our measurement of the fibers' diameter of 320 nm. Using a typical length of $l = 10$ µm between fiber cross-links gives a value of $\kappa \approx 2.4 \times 10^{-6}$. A point force is applied to the node nearest to the center of the model domain. To account for the highly nonlinear geometry, the explicit solver is used with a computational damping that is selected to give the steady-state displacement field that satisfies static force equilibrium. The displacement in the direction of the load is recorded, and the procedure is repeated for different loads to assemble a force–displacement curve. Curves are generated for various different random network geometries. Simulations are performed in dimensionless units and converted to real values using the values described.

To account for a wide range of possible values of $\kappa_b$ and $\kappa_s$, we also performed the simulation for $\kappa = 2 \times 10^{-8}$ and $2 \times 10^{-5}$. A value of $\kappa \approx 2 \times 10^{-8}$ is calculated using the ~40-µm persistence length of fibrin and a softer, 2-MPa Young's modulus reported for fibers in gels formed in the absence of Factor XIII (Collet *et al.*, 2005). A value of $\kappa \approx 2 \times 10^{-5}$ is calculated when $\kappa_b$ is derived by treating each element as a uniform rod of diameter 320 nm of Young's modulus 14.5 MPa (Collet *et al.*, 2005).

### Velocity and deformation representation

For creation of the volumetric reconstruction images in Figure 2, vertex coordinates (as described in *Cell surface rendering*) and their associated scalar or 2D (in the case of Figure 2F) values were saved as .dat files and exported to Tecplot 360, where volume visualization and streamline generation were performed.

Quiver plots were generated in MATLAB with custom code, with the color depicting the angle of fibrin deformation in the *xy*-plane.

The α-actinin-1 velocities mapped onto the cell surface in Figure 4C were generated as follows. The cell surface was determined from the α-actinin-1 signal as described in *Cell surface rendering*. The velocities of α-actinin-1 puncta were determined in three dimensions as described in *Paxillin tracking and α-actinin-1 tracking*. α-Actinin-1 velocities at each vertex in the cell surface were determined as inverse distance-weighted 3D velocities of tracked α-actinin-1 spots within a 2-µm radius. Velocities assigned to each vertex were exported to Tecplot 360 for visualization.

### Paxillin tracking and α-actinin-1 tracking

Paxillin and/or α-actinin-1 signals were bandpass filtered to a passband corresponding to ~0.5–2 µm (paxillin) or ~0.25–1 µm (α-actinin), followed by a subtraction of the resulting extracellular background signal from each slice of each frame of the image.

Tracking was performed in ImageJ on this preprocessed image through the TrackMate plug-in using the LoG detector for 2-µm (paxillin) or 1-µm (α-actinin) spots to detect adhesions/puncta in three dimensions. Spot links were exported to MATLAB for further analysis with custom code.

### Determination of velocity from tracking data

Because the presence of localization error systematically increases the measured displacement relative to the true displacement during particle tracking (Churchman *et al.*, 2005, 2006), reported mean velocities of paxillin, α-actinin, and zyxin from particle tracking were determined from displacement distances corrected as described in the Supplemental Discussion, Characterization of localization error contribution to velocity and determination of robust time resolution for velocity reporting. Linking of spots in TrackMate was performed at the time resolution of imaging (using every time point), but velocities were calculated from start and end points of spots separated by a time delay of 10 ± 1 min, with the exception of Figure 4A and Supplemental Table S1.

The comparison of fibrin velocity (tracked with DVC) to colocalized paxillin plaque velocity or α-actinin velocity was performed as follows. FIDVC was performed on the fibrin channel to get a map of fiber displacements. Tracking of fibrin displacement with paxillin expression was performed on frames 10 ± 1 min apart. Tracking of fibrin displacement with α-actinin-1 expression was performed on frames 3.4–6 min apart. Paxillin or α-actinin-1 was tracked with TrackMate, and the outputs were loaded into MATLAB. Fibrin velocities at the pixels corresponding to the centroids of the tracked paxillin/α-actinin-1 complexes were extracted from the fibrin tracking. Care was taken to calculate paxillin/α-actinin-1 velocities at the time resolution used for fibrin FIDVC tracking. These fibrin velocities and the associated paxillin/α-actinin-1 velocities were saved and used for histograms in Supplemental Figure S3, B and C, and Figure 4A.

Histograms report the distribution of measured and uncorrected velocities determined at a time resolution of 10 ± 1 min, with the exception of Figure 4A and Supplemental Table S1.This suppresses localization noise and masks smaller, nonpersistent velocity fluctuations in the tracked complexes. Histograms comparing velocities between two proteins report velocities determined from the same population of cells and at the same temporal subsampling.

Data in rose plots to describe the angle between vectors were calculated for tracks at a time resolution of 10 ± 1 min, with the exception of Figure 4A. The angle between the vectors in the *xy* (nonoptical) plane is represented in rose plots.

### Quantification of the differential velocity between EGFP–α-actinin-1 puncta and focal adhesions

We determined the rate of addition of new material to stress fibers as follows in cells dually expressing RFP-zyxin and EGFP-α-actinin-1. Tracking of zyxin plaques and α-actinin-1 spots was performed in TrackMate, and tracks were imported into MATLAB. Tracks were sampled to a time resolution of 10 ± 1 min. Zyxin tracks were linked to the closest α-actinin-1 track within 0.5 µm. The 3D velocity vectors were subtracted from each other, as shown in Supplemental Figure S15B. A scalar subtraction (the difference in speed of colocalized puncta and plaques) was also performed to provide a lower bound on the relative velocities.

### Cell migration quantification

Cells transfected with pEGFP-N1–α-actinin-1 and pCMV-LifeAct-TagRFP were embedded in a fibrin gel as described. Imaging started 9 h after gel preparation and was performed at 20× magnification with tiling to collect data for 20+ cells for 2 h. Visibly migrating cells were segmented out of the movie, and crops surrounding these cells were imported into MATLAB. Cells were classified as migratory if the center of mass of the masked cell moved >30 µm between the first and last time points of imaging. This analysis resulted in 8 of 52 cells classified as migratory.

A supplementary analysis was performed on nontransfected cells with phase contrast imaging. Cells were embedded in a gel, and imaged starting 10 h after gel preparation for 4 h. Cells that were spread in the gel at the start of imaging were determined to be migratory if there existed two time points in the time lapse with no cell body overlap. Cells in focus with the coverslip, cells crawling on top of the gel, and cells that divided in this period of time were excluded from the analysis.

### Statistics

All reported velocities are the mean, and reported error is the SEM determined from $10^4$ bootstrap iterations. The *p* values testing distributions were calculated from $10^4$ permutations in a permutation test.

Individual cells were selected for analysis if expression of the fluorescent protein was sufficiently high to result in qualitatively robust tracking.

All experiments reflect data from two or more technical replicates (experiments prepared and imaged on different days).

### Code availability

Code for running FIDVC can be accessed at https://github.com/FranckLab/FIDVC. Code for analyzing fibrin displacement data and analyzing cell signals will be supplied upon request by contacting A.R.D. MATLAB is required to run all code.

## ACKNOWLEDGMENTS

We gratefully acknowledge Cedric Espenel and Jon Mulholland at the Stanford Cell Sciences Imaging facility and Andrew Olson at the Neuroscience Microscopy Service Center for assistance in live-cell imaging. We thank Gerald Fuller, Louise Jawerth, Sam Stanwyck, and Joe Barakat for technical discussion. This work is supported by National Institutes of Health New Innovator Award DP2-OD007078-01 and Award R01-GM112998-01 (A.R.D.), a Stanford Cardiovascular Institute Seed Grant (A.R.D.), a Stanford Graduate Fellowship (A.S.A.), National Institutes of Health/National Human Genome Research Institute T32 HG000044 Award (L.M.O.), National Institutes of Health T32 GM08294 Award (L.M.O.), and a National Science Foundation Graduate Research Fellowship (L.M.O.). M.P. gratefully acknowledges support from a Brown University Graduate Fellowship. Part of this work was performed at the Stanford Nano Shared Facilities, which is supported by the National Science Foundation under Award ECCS-1542152.

## REFERENCES

Abhilash AS, Baker BM, Trappmann B, Chen CS, Shenoy VB (2014). Remodeling of fibrous extracellular matrices by contractile cells: predictions from discrete fiber network simulations. Biophys J 107, 1829–1840.

Alexandrova AY, Arnold K, Schaub S, Vasiliev JM, Meister JJ, Bershadsky AD, Verkhovsky AB (2008). Comparative dynamics of retrograde actin flow and focal adhesions: formation of nascent adhesions triggers transition from fast to slow flow. PLoS One 3, e3234.

Aratyn-Schaus Y, Gardel ML (2010). Transient frictional slip between integrin and the ECM in focal adhesions under myosin II tension. Curr Biol 20, 1145–1153.

Baker BM, Trappmann B, Wang WY, Sakar MS, Kim IL, Shenoy VB, Burdick JA, Chen CS (2015). Cell-mediated fibre recruitment drives extracellular matrix mechanosensing in engineered fibrillar microenvironments. Nat Mater 14, 1262–1268.

Bangasser BL, Rosenfeld SS, Odde DJ (2013). Determinants of maximal force transmission in a motor-clutch model of cell traction in a compliant microenvironment. Biophys J 105, 581–592.

Bar-Kochba E, Toyjanova J, Andrews E, Kim KS, Franck C (2015). A fast iterative digital volume correlation algorithm for large deformations. Exp Mech 55, 261–274.

Bhatt A, Kaverina I, Otey C, Huttenlocher A (2002). Regulation of focal complex composition and disassembly by the calcium-dependent protease calpain. J Cell Sci Suppl 115, 3415–3425.

Bloom RJ, George JP, Celedon A, Sun SX, Wirtz D (2008). Mapping local matrix remodeling induced by a migrating tumor cell using three-dimensional multiple-particle tracking. Biophys J 95, 4077–4088.

Brown CM, Hebert B, Kolin DL, Zareno J, Whitmore L, Horwitz AR, Wiseman PW (2006). Probing the integrin-actin linkage using high-resolution protein velocity mapping. J Cell Sci Suppl 119, 5204–5214.

Burnette DT, Manley S, Sengupta P, Sougrat R, Davidson MW, Kachar B, Lippincott-Schwartz J (2011). A role for actin arcs in the leading-edge advance of migrating cells. Nat Cell Biol 13, 371–381.

Burridge K, Wittchen ES (2013). The tension mounts: stress fibers as force-generating mechanotransducers. J Cell Biol 200, 9–19.

Chan CE, Odde DJ (2008). Traction dynamics of filopodia on compliant substrates. Science 322, 1687–1691.

Charras G, Paluch E (2008). Blebs lead the way: how to migrate without lamellipodia. Nat Rev Mol Cell Biol 9, 730–736.

Chaudhuri O, Gu L, Darnell M, Klumpers D, Bencherif SA, Weaver JC, Huebsch N, Mooney DJ (2015). Substrate stress relaxation regulates cell spreading. Nat Commun 6, 1–7.

Chiu C-L, Digman MA, Gratton E (2013). Measuring actin flow in 3D cell protrusions. Biophys J 105, 1746–1755.

Churchman LS, Flyvbjerg H, Spudich JA (2005). Single molecule high-resolution colocalization of Cy3 and Cy5 attached to macromolecules measures intramolecular distances through time. Proc Natl Acad Sci USA 102, 1419–1423.

Churchman SL, Flyvbjerg H, Spudich JA (2006). A non-Gaussian distribution quantifies distances measured with fluorescence localization techniques. Biophys J 90, 668–671.

Clark RA, Lanigan JM, DellaPelle P, Manseau E, Dvorak HF, Colvin RB (1982). Fibronectin and fibrin provide a provisional matrix for epidermal cell migration during wound reepithelialization. J Invest Dermatol 79, 264–269.

Collet JP, Shuman H, Ledger RE, Lee S, Weisel JW (2005). The elasticity of an individual fibrin fiber in a clot. Proc Natl Acad Sci USA 102, 9133–9137.

Cukierman E, Pankov R, Stevens DR, Yamada KM (2001). Taking cell-matrix adhesions to the third dimension. Science 294, 1708–1712.

Desbrun M, Meyer M, Schröder P, Barr AH (1999). Implicit fairing of irregular meshes using diffusion and curvature flow. In: Proceedings of the 26th Annual Conference on Computer Graphics and Interactive Techniques—SIGGRAPH'99, New York: ACM Press, 317–324.

Doyle AD, Carvajal N, Jin A, Matsumoto K, Yamada KM (2015). Local 3D matrix microenvironment regulates cell migration through spatiotemporal dynamics of contractility-dependent adhesions. Nat Commun 6, 8720.

Doyle AD, Yamada KM (2016). Mechanosensing via cell-matrix adhesions in 3D microenvironments. Exp Cell Res 343, 60–66.

Duong H, Wu B, Tawil B (2009). Modulation of 3D fibrin matrix stiffness by intrinsic fibrinogen-thrombin compositions and by extrinsic cellular activity. Tissue Eng Part A 15, 1865–1876.

Elosegui-Artola A, Oria R, Chen Y, Kosmalska A, Pérez-González C, Castro N, Zhu C, Trepat X, Roca-Cusachs P (2016). Mechanical regulation of a molecular clutch defines force transmission and transduction in response to matrix rigidity. Nat Cell Biol 18, 540–548.

Farid H, Simoncelli EP (2004). Differentiation of discrete multidimensional signals. IEEE Trans Image Process 13, 496–508.

Franck C, Maskarinec SA, Tirrell DA, Ravichandran G (2011). Three-dimensional traction force microscopy: a new tool for quantifying cell-matrix interactions. PLoS One 6, e17833.

Gabbiani G, Hirschel BJ, Ryan GB, Statkov PR, Majno G (1972). Granulation tissue as a contractile organ. a study of structure and function. J Exp Med 135, 719–734.

Gardel ML, Sabass B, Ji L, Danuser G, Schwarz US, Waterman CM (2008). Traction stress in focal adhesions correlates biphasically with actin retrograde flow speed. J Cell Biol 183, 999–1005.

Gardel ML, Schneider IC, Aratyn-Schaus Y, Waterman CM (2010). Mechanical integration of actin and adhesion dynamics in cell migration. Annu Rev Cell Dev Biol 26, 315–533.

Giannone G, Dubin-Thaler BJ, Dobereiner H-G, Kieffer N, Bresnick AR, Sheetz MP (2004). Periodic lamellipodial contractions correlate with rearward actin waves. Cell 116, 431–443.

Giannone G, Dubin-Thaler BJ, Rossier O, Cai Y, Chaga O, Jiang G, Beaver W, Dobereiner H-G, Freund Y, Borisy G, Sheetz MP (2007). Lamellipodial actin mechanically links myosin activity with adhesion-site formation. Cell 128, 561–575.
Giri A, Bajpai S, Trenton N, Jayatilaka H, Longmore GD, Wirtz D (2013). The Arp2/3 complex mediates multigeneration dendritic protrusions for efficient 3-dimensional cancer cell migration. FASEB J 27, 4089–4099.
Grinnell F (1994). Fibroblasts, myofibroblasts, and wound contraction. J Cell Biol 124, 401–404.
Grinnell F, Petroll WM (2010). Cell motility and mechanics in three-dimensional collagen matrices. Annu Rev Cell Dev Biol 26, 335–361.
Hakkinen KM, Harunaga JS, Doyle AD, Yamada KM (2011). Direct comparisons of the morphology, migration, cell adhesions, and actin cytoskeleton of fibroblasts in four different three-dimensional extracellular matrices. Tissue Eng Part A 17, 713–724.
Harris AK, Wild P, Stopak D (1980). Silicone rubber substrata: a new wrinkle in the study of cell locomotion. Science 208, 177–179.
Head DA, Levine AJ, MacKintosh FC (2003). Distinct regimes of elastic response and deformation modes of cross-linked cytoskeletal and semiflexible polymer networks. Phys Rev E Stat Nonlin Soft Matter Phys 68, 61907.
Hinz B (2012). Mechanical aspects of lung fibrosis: a spotlight on the myofibroblast. Proc Am Thorac Soc 9, 137–147.
Hotulainen P, Lappalainen P (2006). Stress fibers are generated by two distinct actin assembly mechanisms in motile cells. J Cell Biol 173, 383–394.
Hu K, Ji L, Applegate KT, Danuser G, Waterman-Storer CM (2007). Differential transmission of actin motion within focal adhesions. Science 315, 111–115.
Jansen KA, Bacabac RG, Piechocka IK, Koenderink GH (2013). Cells actively stiffen fibrin networks by generating contractile stress. Biophys J 105, 2240–2251.
Khatau SB, Bloom RJ, Bajpai S, Razafsky D, Zang S, Giri A, Wu P-H, Marchand J, Celedon A, Hale CM, *et al.* (2012). The distinct roles of the nucleus and nucleus-cytoskeleton connections in three-dimensional cell migration. Sci Rep 2, 488.
Kim MC, Whisler J, Silberberg YR, Kamm RD, Asada HH (2015). Cell invasion dynamics into a three dimensional extracellular matrix fibre network. PLoS Comput Biol 11, 1–29.
Koch TM, Münster S, Bonakdar N, Butler JP, Fabry B (2012). 3D traction forces in cancer cell invasion. PLoS One 7, e33476.
Krieg M, Arboleda-Estudillo Y, Puech P-H, Käfer J, Graner F, Müller DJ, Heisenberg C-P (2008). Tensile forces govern germ-layer organization in zebrafish. Nat Cell Biol 10, 429–436.
Kubow KE, Conrad SK, Horwitz AR (2013). Matrix microarchitecture and myosin II determine adhesion in 3D matrices. Curr Biol 23, 1607–1619.
Kubow KE, Horwitz AR (2011). Reducing background fluorescence reveals adhesions in 3D matrices. Nat Cell Biol 13, 3–5.
Legant WR, Miller JS, Blakely BL, Cohen DM, Genin GM, Chen CS (2010). Measurement of mechanical tractions exerted by cells in three-dimensional matrices. Nat Methods 7, 969–971.
Lesman A, Notbohm J, Tirrell DA, Ravichandran G (2014). Contractile forces regulate cell division in three-dimensional environments. J Cell Biol 205, 155–162.
Lin C, Forscher P (1995). Growth cone advance is inversely proportional to retrograde F-actin flow. Neuron 14, 763–771.
Livne A, Geiger B (2016). The inner workings of stress fibers—from contractile machinery to focal adhesions and back. J Cell Sci 129, 1293–1304.
Mammoto T, Mammoto A, Ingber DE (2013). Mechanobiology and developmental control. Annu Rev Cell Dev Biol 29, 27–61.
Mekhdjian AH, Kai F, Rubashkin MG, Prahl LS, Przybyla M, McGregor AL, Bell ES, Barnes M, DuFort CC, Ou G, *et al.* (2017). Integrin-mediated traction force enhances paxillin molecular associations and adhesion dynamics that increase the invasiveness of tumor cells into a three-dimensional extracellular matrix. Mol Biol Cell 28, 1467–1488.
Meshel AS, Wei Q, Adelstein RS, Sheetz MP (2005). Basic mechanism of three-dimensional collagen fibre transport by fibroblasts. Nat Cell Biol 7, 157–164.
Mochitate K, Pawelek P, Grinnell F (1991). Stress relaxation of contracted collagen gels: disruption of actin filament bundles, release of cell surface fibronectin, and down-regulation of DNA and protein synthesis. Exp Cell Res 193, 198–207.
Notbohm J, Lesman A, Rosakis P, Tirrell DA, Ravichandran G (2015a). Microbuckling of fibrin provides a mechanism for cell mechanosensing. J R Soc Interface 12, 20150320.
Notbohm J, Lesman A, Tirrell DA, Ravichandran G (2015b). Quantifying cell-induced matrix deformation in three dimensions based on imaging matrix fibers. Integr Biol (Camb) 7, 1186–1195.
Novikova EA, Storm C (2013). Contractile fibers and catch-bond clusters: a biological force sensor? Biophys J 105, 1336–1345.
Oakes PW, Beckham Y, Stricker J, Gardel ML (2012). Tension is required but not sufficient for focal adhesion maturation without a stress fiber template. J Cell Biol 196, 363–374.
Oliver T, Dembo M, Jacobson K (1995). Traction forces in locomoting cells. Cell Motil Cytoskeleton 31, 225–240.
Onck PR, Koeman T, Van Dillen T, Van Der Giessen E (2005). Alternative explanation of stiffening in cross-linked semiflexible networks. Phys Rev Lett 95, 19–22.
Pathak A, Kumar S (2012). Independent regulation of tumor cell migration by matrix stiffness and confinement. Proc Natl Acad Sci USA 109, 10334–10339.
Petrie RJ, Koo H, Yamada KM (2014). Generation of compartmentalized pressure by a nuclear piston governs cell motility in a 3D matrix. Science 345, 1062–1065.
Petroll WM, Ma L (2003). Direct, dynamic assessment of cell-matrix interactions inside fibrillar collagen lattices. Cell Motil Cytoskeleton 55, 254–264.
Piechocka IK, Bacabac RG, Potters M, Mackintosh FC, Koenderink GH (2010). Structural hierarchy governs fibrin gel mechanics. Biophys J 98, 2281–2289.
Plotnikov SV, Pasapera AM, Sabass B, Waterman CM (2012). Force fluctuations within focal adhesions mediate ECM-rigidity sensing to guide directed cell migration. Cell 151, 1513–1527.
Ponti A, Machacek M, Gupton SL, Waterman-Storer CM, Danuser G (2004). Two distinct actin networks drive the protrusion of migrating cells. Science 305, 1782–1786.
Ritter AT, Asano Y, Stinchcombe JC, Dieckmann NMG, Chen BC, Gawden-Bone C, van Engelenburg S, Legant W, Gau L, Davidson MW, *et al.* (2015). Actin depletion initiates events leading to granule secretion at the immunological synapse. Immunity 42, 864–876.
Salmon WC, Adams MC, Waterman-Storer CM (2002). Dual-wavelength fluorescent speckle microscopy reveals coupling of microtubule and actin movements in migrating cells. J Cell Biol 158, 31–37.
Schäfer M, Werner S (2008). Cancer as an overhealing wound: an old hypothesis revisited. Nat Rev Mol Cell Biol 9, 628–638.
Schwartz MA, Chen CS (2013). Cell biology. Deconstructing dimensionality. Science 339, 402–404.
Schwarz US, Erdmann T, Bischofs IB (2006). Focal adhesions as mechanosensors: the two-spring model. BioSystems 83, 225–232.
Skau CT, Plotnikov SV, Doyle AD, Waterman CM (2015). Inverted formin 2 in focal adhesions promotes dorsal stress fiber and fibrillar adhesion formation to drive extracellular matrix assembly. Proc Natl Acad Sci USA 112, 2447–2256.
Starke J, Maaser K, Wehrle-haller B, Friedl P (2013). Mechanotransduction of mesenchymal melanoma cell invasion into 3D collagen lattices: filopod-mediated extension. relaxation cycles and force anisotropy. Exp Cell Res 319, 2424–2433.
Steinwachs J, Metzner C, Skodzek K, Lang N, Thievessen I, Mark C, Münster S, Aifantis KE, Fabry B (2016). Three-dimensional force microscopy of cells in biopolymer networks. Nat Methods 13, 171–176.
Stout DA, Bar-Kochba E, Estrada JB, Toyjanova J, Kesari H, Reichner JS, Franck C (2016). Mean deformation metrics for quantifying 3D cell. matrix interactions without requiring information about matrix material properties. Proc Natl Acad Sci USA 113, 2898–2903.
Tamariz E, Grinnell F (2002). Modulation of fibroblast morphology and adhesion during collagen matrix remodeling. Mol Biol Cell 13, 3915–3929.
Tee YH, Shemesh T, Thiagarajan V, Hariadi RF, Anderson KL, Page C, Volkmann N, Hanein D, Sivaramakrishnan S, Kozlov MM, Bershadsky AD (2015). Cellular chirality arising from the self-organization of the actin cytoskeleton. Nat Cell Biol 17, 445–457.
Thievessen I, Fakhri N, Steinwachs J, Kraus V, McIsaac RS, Gao L, Chen BC, Baird MA, Davidson MW, Betzig E, *et al.* (2015). Vinculin is required for cell polarization, migration, and extracellular matrix remodeling in 3D collagen. FASEB J 29, 4555–4567.
Tinevez J-Y, Perry N, Schindelin J, Hoopes GM, Reynolds GD, Laplantine E, Bednarek SY, Shorte SL, Eliceiri KW (2016). TrackMate: an open and extensible platform for single-particle tracking. Methods 115, 80–90.
To WS, Midwood KS (2011). Plasma and cellular fibronectin: distinct and independent functions during tissue repair. Fibrogenesis Tissue Repair 4, 21.
Tojkander S, Gateva G, Husain A, Krishnan R, Lappalainen P (2015). Generation of contractile actomyosin bundles depends on mechanosensitive actin filament assembly and disassembly. Elife 4, 1–28.

Tomasek JJ, Gabbiani G, Hinz B, Chaponnier C, Brown RA (2002). Myofibroblasts and mechano-regulation of connective tissue remodelling. Nat Rev Mol Cell Biol 3, 349–363.
Tomasek JJ, Haaksma CJ, Eddy RJ, Vaughan MB (1992). Fibroblast contraction occurs on release of tension in attached collagen lattices: dependency on an organized actin cytoskeleton and serum. Anat Rec 232, 359–368.
Toyjanova J, Flores-Cortez E, Reichner JS, Franck C (2015). Matrix confinement plays a pivotal role in regulating neutrophil-generated tractions, speed, and integrin utilization. J Biol Chem 290, 3752–3763.
Toyjanova J, Hannen E, Bar-Kochba E, Darling EM, Henann DL, Franck C (2014). 3D viscoelastic traction force microscopy. Soft Matter 10, 8095–8106.
Vishwanath M, Ma L, Otey CA, Jester JV, Petroll WM (2003). Modulation of corneal fibroblast contractility within fibrillar collagen matrices. Invest Ophthalmol Vis Sci 44, 4724–4735.
Waterman-Storer CM, Desai A, Bulinski JC, Salmon ED (1998). Fluorescent speckle microscopy, a method to visualize the dynamics of protein assemblies in living cells. Curr Biol 8, 1227–1231.
Winer JP, Oake S, Janmey PA (2009). Non-linear elasticity of extracellular matrices enables contractile cells to communicate local position and orientation. PLoS One 4, e6382.
Wozniak MA, Chen CS (2009). Mechanotransduction in development: a growing role for contractility. Nat Rev Mol Cell Biol 10, 34–43.
Wu Z, Plotnikov SV, Moalim AY, Waterman CM, Liu J (2017). Two distinct actin networks mediate traction oscillations to confer focal adhesion mechanosensing. Biophys J 112, 780–794.